

**LASER MATERIALS AND TECHNOLOGY RESEARCH CENTER OF  
GENERAL PHYSICS INSTITUTE**

**Final report**

**Contract SPC 99-4061**

**«COLOR CENTER MOCKUP DEVELOPMENT AND  
TESTING»**

**Moscow**

**March 2001**

## Form SF298 Citation Data

<b>Report Date</b> <i>("DD MON YYYY")</i> 00032001	<b>Report Type</b> N/A	<b>Dates Covered (from... to)</b> <i>("DD MON YYYY")</i>
<b>Title and Subtitle</b> Color Center Mockup Development and Testing		<b>Contract or Grant Number</b>
		<b>Program Element Number</b>
<b>Authors</b> Basiev, Tasoltan Tazretovich		<b>Project Number</b>
		<b>Task Number</b>
		<b>Work Unit Number</b>
<b>Performing Organization Name(s) and Address(es)</b> General Physics Institute 38 Vavilov St Moscow 117942 Russia		<b>Performing Organization Number(s)</b>
<b>Sponsoring/Monitoring Agency Name(s) and Address(es)</b> EOARD PSC 802 BOX 14 FPO 09499-0200		<b>Monitoring Agency Acronym</b>
		<b>Monitoring Agency Report Number(s)</b>
<b>Distribution/Availability Statement</b> Approved for public release, distribution unlimited		
<b>Supplementary Notes</b>		
<b>Abstract</b>		
<b>Subject Terms</b>		
<b>Document Classification</b> unclassified	<b>Classification of SF298</b> unclassified	
<b>Classification of Abstract</b> unclassified	<b>Limitation of Abstract</b> unlimited	
<b>Number of Pages</b> 60		

REPORT DOCUMENTATION PAGE			Form Approved OMB No. 0704-0188	
Public reporting burden for this collection of information is estimated to average 1 hour per response, including the time for reviewing instructions, searching existing data sources, gathering and maintaining the data needed, and completing and reviewing the collection of information. Send comments regarding this burden estimate or any other aspect of this collection of information, including suggestions for reducing this burden to Washington Headquarters Services, Directorate for Information Operations and Reports, 1215 Jefferson Davis Highway, Suite 1204, Arlington, VA 22202-4302, and to the Office of Management and Budget, Paperwork Reduction Project (0704-0188), Washington, DC 20503.				
1. AGENCY USE ONLY (Leave blank)		2. REPORT DATE  March 2001		3. REPORT TYPE AND DATES COVERED  Final Report
4. TITLE AND SUBTITLE  Color Center Mockup Development and Testing			5. FUNDING NUMBERS  F61775-99-WE	
6. AUTHOR(S)  Prof Tasoltan Tazretovich Basiev				
7. PERFORMING ORGANIZATION NAME(S) AND ADDRESS(ES)  General Physics Institute 38 Vavilov St Moscow 117942 Russia			8. PERFORMING ORGANIZATION REPORT NUMBER  N/A	
9. SPONSORING/MONITORING AGENCY NAME(S) AND ADDRESS(ES)  EOARD PSC 802 BOX 14 FPO 09499-0200			10. SPONSORING/MONITORING AGENCY REPORT NUMBER  SPC 99-4061	
11. SUPPLEMENTARY NOTES				
12a. DISTRIBUTION/AVAILABILITY STATEMENT  Approved for public release; distribution is unlimited.			12b. DISTRIBUTION CODE  A	
13. ABSTRACT (Maximum 200 words)  This report results from a contract tasking General Physics Institute as follows: The contractor will develop and test a narrow linewidth (~500 MHz), tunable (1080 to 1350 nm) color center laser based on LiF and NaF crystals with a goal of being 10 to 20% efficient when pumped with a Nd:YAG or Nd:LaF3 laser.				
14. SUBJECT TERMS  EOARD, Tunable lasers, Narrow linewidth lasers, Solid state lasers			15. NUMBER OF PAGES  59	
			16. PRICE CODE  N/A	
17. SECURITY CLASSIFICATION OF REPORT  UNCLASSIFIED	18. SECURITY CLASSIFICATION OF THIS PAGE  UNCLASSIFIED	19. SECURITY CLASSIFICATION OF ABSTRACT  UNCLASSIFIED	20. LIMITATION OF ABSTRACT  UL	

## Content:

### Introduction

1. Active element of color center lasers
  - 1.1. Physicochemical, mechanical and optical characteristics of the crystal hosts for active elements of color center lasers.
  - 1.2. Types of color centers in ionic crystals
  - 1.3. Color center formation in alkali-halide crystals
  - 1.4.  $\text{LiF:F}_2^-$  active element optimization
  - 1.5.  $\text{LiF:F}_2^-$  crystals laser characterization
  - 1.6. NaF color center crystal optical and laser characteristics
2. Optical scheme of color center oscillator.
  - 2.1.  $\text{LiF:F}_2^-$  color center active element
  - 2.2. Dichroic intracavity mirror
  - 2.3. Sine mechanism for diffraction grating scanning
  - 2.4. Prism telescope
  - 2.5. Prism and mirror holder
  - 2.6. Fabri Perrot etalon
  - 2.7. Output coupler mirror
3. Color center energy and power amplifier
  - 3.1.  $\text{LiF:F}_2^-$  amplifier with  $\text{Nd}^{3+}$ :YAG pumping
  - 3.2.  $\text{LiF:F}_2^-$  double-pass amplifier with  $\text{Nd}^{3+}$ :YLiF<sub>4</sub> pump laser

### References

## Introduction

The research and development of all solid-state laser system broadly tunable in 0.9 - 1.5  $\mu\text{m}$  spectral range with high output energy and narrow oscillating line is a complex problem of laser physics, which includes solution of several scientific and technical tasks:

1. Development of laser active element from Color Center crystals, including
  - 1.1. physicochemical, mechanical and optical characteristics of crystal hosts for active elements of color center lasers;
  - 1.2. color center formation in alkali-halide crystals under ionizing irradiation;
  - 1.3. optimization of color center crystal optical properties for laser operation.
2. Study and optimization of oscillator cavity optical scheme for narrow line operation, including
3. Study, optimization and development of high power amplifier for narrow line color center laser system.

Laser active  $\text{F}_2^-$  and  $\text{F}_3^-$  color centers are aggregate quasi-molecular vacancies capturing 3 or 4 electrons. Luminescence spectrum of  $\text{F}_2^-$  color centers in LiF crystal at room temperature covers very wide spectral range from 0.95 to 1.35  $\mu\text{m}$ . Its absorption band extends from 0.8 to 1.13  $\mu\text{m}$  and overlaps well with the radiation of well developed Nd laser sources [1,2]. In the previous work it was shown that high thermo and physical properties of LiF crystals (see Table 1.1) allowed them to operate with high energy and pump densities up to 100 J and 2  $\text{J}/\text{cm}^2$  [3]. In Ref. [4] the intracavity operation of  $\text{LiF}:\text{F}_2^-$  laser with 15 J output power and 75 % optical efficiency was demonstrated. Small change in the pumping wavelength from 1064 to 1047 nm results in two times increase of Color Center Laser (CCL) efficiency.

Investigation of narrow line oscillation of CCL was aimed on the development of smoothly and continuously tunable laser for near IR spectral region. The cavity for narrow line oscillation was composed with one or two diffraction gratings. The first grating worked at a grazing incident angle as an intracavity telescope, spectral selector and output coupler; and the second, mirror grating worked in the auto-collimation regime for additional spectral selectivity. This scheme provided continuously tunable radiation of  $\text{LiF}:\text{F}_2^-$  laser with stable narrow line width of less than  $0.03 \text{ cm}^{-1}$  and conversion efficiency 10-15% [1,2].

Previously developed tunable CCLs provide tunable radiation in wide spectral region for  $\text{LiF}:\text{F}_2^-$  from 1080 till 1270 nm with maximum conversion efficiency about 20% and for

NaF:F<sub>3</sub><sup>-</sup> from 1100 to 1340 nm with efficiency up to 10% with 1064 nm Nd<sup>3+</sup>:YAG pumping. As a spectral selective element, the optical cavity includes diffraction grating, working in auto-collimating scheme with the output in the zero diffraction order. The scheme provides the linewidth of 1÷3 cm<sup>-1</sup>. The optional second selective element, Fabri-Perrot etalon with different finesse, narrows the spectral line to 0.3 cm<sup>-1</sup> with output efficiency decreasing by a factor of 1.5-2. This laser has manual and computer controlled wavelength tuning and a helium-neon laser for wavelength adjustment and laser cavity alignment.

The new narrow line powerful Color Center mockup will include mechanical base, optical mechanical mounts with adjustable optical elements (lenses, mirrors, and telescopes), two sets of Color Center laser crystals, two precision scanning modules with stepping motors for gratings and etalon scanning controlled by computer.

*The goal of the project* was to develop and test a narrow linewidth high energy color center laser mockup based on two types of color center crystals: LiF:F<sub>2</sub><sup>-</sup> and NaF:F<sub>3</sub><sup>-</sup> with a very wide tuning range from 1.08 to 1.35 μm. As a result, high energy fixed frequency radiation of Nd-solid state laser will be converted into narrow line (Δν~500 MHz) laser radiation tunable in extremely broad spectral range 1.08 - 1.35 μm.

## 1. Active element of color center lasers

### 1.1. *Physicochemical, mechanical and optical characteristics of the crystal hosts for active elements of color center lasers*

Color centers exist in many types of crystalline solids, including both ionic and covalently bonded lattices. Below (see Table 1.1) the major physicochemical, optical and mechanical characteristics of the crystal hosts intended for CC laser-active elements are considered and compared with each other and with well known laser media. The most promising for developing color centers are crystals of alkali-halide metals, alkali-earth fluorides, oxides (for instance, sapphire) and covalent crystals (at present the only available representative is diamond).

The most wide-spread media with color centers - alkali-halide crystals - are optically transparent in a wide spectrum range from 0.11-0.25 to 7-35  $\mu\text{m}$  and are widely used as optical materials for instruments of UV, visible and IR optical technology, optics and spectroscopy. The structure of the alkali-halide crystals refers to the Fm3m spatial group with a general cubic symmetry of the crystal lattice. Thus, the alkali-halide crystals are inherently isotropic, i.e. their refraction index does not depend upon polarization and direction of light propagation. A simple, fast and available Kirpulos technique enables to grow high-quality crystals with large cross section and volumes (for instance,  $\varnothing 400 \times 200$  mm) on a high-scale commercial level. The crystal media so grown may be used for fabrication of large active elements and Q-switches in powerful laser systems.

The LiF and NaF crystals are most, outstanding among alkali-halides for their low hygroscopicity. Their solubility in water is rather low and acceptable for practical applications in natural conditions. It is already expedient to use sodium fluoride crystals in a dried atmosphere. All the rest alkali-halide crystals without fail can't be used in the damp air. Their facets become matt without special protective coating.

Of the alkali-halides LiF crystals have the smallest (close to  $-1.2 \cdot 10^{-5} \text{ }^\circ\text{C}^{-1}$ ) value of temperature-derivative refractive index and a high thermal conductivity coefficient ( $14 \text{ W} \cdot \text{m}^{-1} \cdot \text{C}^{-1}$  at 300 K, even higher than the value of  $13 \text{ W} \cdot \text{m}^{-1} \cdot \text{C}^{-1}$  of YAG crystal). Thus, the critical thermal power  $P_{cr}$  ( $P_{cr} = \lambda K |dn/dt|^{-1}$ ) of a LiF crystal [1, 2, 7], for which the value of thermal aberration becomes comparable with the laser wavelength amounts to 1.25 W at  $\lambda = 1.06 \text{ } \mu\text{m}$  (for YAG:Nd<sup>3+</sup>  $P_{cr}=1.3\text{W}$ ). Therefore one can consider LiF as a promising laser

lattice for high average power laser operation at room temperature. A comparatively small nonlinear refractive index value  $n_2$  for LiF provides, a high level of self-focusing critical power – 0.46 MW, ( $P_{cr}^s = \varepsilon_o C \lambda^2 / 8\pi n_2$ ) - which exceeds the  $P_{cr}^s$  of YAG crystals (0.30 MW) and is slightly lower than for ED-2 glass ( $P_{cr}^s = 0.69$  MW). From this point of view as well as due to a high, comparable to YAG crystal, laser induced bulk damage threshold of 3.6 GW/cm<sup>2</sup> (at 1.06  $\mu$ m for 10 ns pulses) LiF crystals are considered as prospective lattices for developing active elements of CCL and amplifiers of powerful laser systems.

As shown in Table 1.1, alkali-halide crystals have low Knupp hardness values, 10-200 times lower than for the Al<sub>2</sub>O<sub>3</sub> and YAG crystals which are most widely used in laser technology. This makes it difficult to achieve and preserve highly polished surfaces for all alkali-halide crystals except LiF and NaF during the process of preparation and application.

The most durable of the alkali-halide crystals - LiF - has a tensile strength almost 20 times less than that for YAG, 10 times less than for laser silica glasses and close to the strength of phosphate glasses. Moreover, alkali-halide crystals easily come to pieces along the [100] cleavage planes under impact. Therefore, they have to be carefully handled during exploitation and protected from appreciable thermal gradients, thermo- and mechanical shocks.

Alkali-earth fluorides are of great interest as host crystals for active media with color centers. They are easily produced to have low hygroscopicity and high mechanical and thermal strength, in contrast to alkali-halide crystals.

Also, promising for application as CC active media are sapphire and diamond. These crystals feature a unique combination of thermal and mechanical properties, which exceed (as seen in Table 1.1) the corresponding values for the YAG crystals. However, they are not so readily accessible for technology as alkali- halides.



Table 1.1. Main physicochemical, mechanical and optical characteristics of the most promising crystal hosts with CCs [2].

Crystal	$\rho$ (g/cm <sup>3</sup> )	$d_o$ ( $\text{\AA}$ )	$H$ (kg/mm <sup>2</sup> )	Solubility (g/100g H <sub>2</sub> O)	$T_m$ (K)	$K$ (W/mK)	$\alpha \times 10^6$ (K <sup>-1</sup> )	$E$ (kg/mm <sup>2</sup> )	$\mu$	$S_T$ (kg/mm <sup>2</sup> )	$R_T^*$ (W/m)	$n$	$dn/dT \times 10^5$ (K <sup>-1</sup> )	$I_{thr} \times 10^{-12}$ (W/m <sup>2</sup> )	Transparency range at $\alpha=1\text{cm}^{-1}$ level
LiF	2.64	4.03	99-102	0.12	1121	14.2	33.7	8,820	0.28	1.2-4.0	43-143	1.387	-2.9	3600	0.11-6.6
NaF	2.79	4.62	60	4.2	1270	9.2	32.2	8,780	0.19	-	-	1.321	-1.8	1400	0.16-11.2
NaCl	2.17	5.64	15.2-18.2	36.0	1074	6.4	39.6	4,360	0.20	-	-	1.53	-3.7	200	0.17-18.0
KF	2.50	5.35	-	94.9	1130	-	-	-	-	-	-	-	-	-	0.2-15.0
KCl	1.99	6.29	7.2-9.3	37.4	1049	6.0	37.0	3,810	0.14	-	-	1.48	-3.3	700	0.18-23.0
KBr	2.75	6.60	6-7	70.9	1007	4.8	38.4	3,290	0.32	-	-	1.54	-3.2	500	0.21-28.0
KI	3.13	7.07	5	144.0	959	2.1	41.2	2,550	0.14	-	-	1.64	-4.5	200	0.3-35.0
RbCl	2.76	6.58	-	94.2	717	-	32.8	-	-	-	-	-	-	-	-
MgF <sub>2</sub>	3.18	a=4.64 c=3.06	576	0.0076	1,536	21 $\perp$ c 30 $\parallel$ c	9.4 $\perp$ c 13.4 $\parallel$ c	17,265	0.27	5.4	470	n <sub>0</sub> =1.373 n <sub>c</sub> =1.385	11.2 5.8	1000	0.1-7.0
CaF <sub>2</sub>	3.18	5.46	120-163	0.0016	1,676	9.7	18.8	14,000	-	-	-	1.429	-1.05	>1000	0.13-9.4
SrF <sub>2</sub>	4.24	5.79	144	<0.1	1,190	-	19.6	-	-	-	-	-	-	-	0.1-9.0
Al <sub>2</sub> O <sub>3</sub>	3.974	a=4.76 c=13.0	2100	0	2,313	35.0	5.0 $\perp$ c 6.7 $\parallel$ c	35,230	0.27	55.0	10,000	n <sub>0</sub> =1.765 n <sub>c</sub> =1.757	1.3 0.97	1900	0.18-5.1
Diamond	3.515	3.57	8820	0	3,770	900.0	1.0	58,000	-	-	-	2.40	0.4	12000	0.24-2.7
Y <sub>3</sub> Al <sub>5</sub> O <sub>12</sub>	4.55	12.0	1350	0	2,223	13.0	7.8	31,275	-	20.0	790	1.815	1.05	2000	0.21-5.3
ED-2 glass	2.539	-	-	-	582	1.4	8.0	9,190	0.24	10.0	140	1.56	0.3	-	-

Thermal shock parameter,  $R$ , characterizes the thermo-mechanical strength of the material. For instance, for a plate element with a thickness  $t$ , thermal power  $P_V$ , which may be absorbed by the medium with a parameter  $R_T$  without being damaged,  $P_V = 12R_T/t^2$ , where  $R_T = S_T(1-\mu)K/\alpha E$ .

Symbols:  $\rho$ , density (g/cm<sup>3</sup>);  $d$ , lattice constant ( $\text{\AA}$ );  $H$ , Knupp hardness (kg/mm<sup>2</sup>);  $T_m$ , melting temperature (K);  $K$ , coefficient of thermal conductivity at 300K (W/m K);  $\alpha$ , coefficient of linear expansion at 300K (K<sup>-1</sup>);  $E$ , Young modulus (kg/mm<sup>2</sup>);  $\mu$ , Poisson's coefficient;  $S$ , compression (tension) or bending strength (kg/mm<sup>2</sup>);  $R$ , thermal shock parameter (W/m);  $n$ , refractive index at  $\lambda=1\mu\text{m}$ ;  $dn/dT$ , temperature derivative refractive index at  $\lambda=1\mu\text{m}$  (K<sup>-1</sup>);  $I_{thr}$ , laser induced bulk damage threshold at  $\lambda=1.06\mu\text{m}$  for 10 ns pulse duration.

## 1.2. Types of color centers in ionic crystals

Fig. 1.1 shows some of the major types of CCs that one can use to achieve stimulated radiation. In general, the major crystals where laser active CCs can be developed are pure and impurity-doped fluorides and chlorides of Li, Na, K, and Rb alkali metals [2, 7-10], as well as  $\text{CaF}_2$  and  $\text{SrF}_2$  [11]. Laser oscillation has also been reported using CCs in  $\text{Al}_2\text{O}_3$  [12, 13], diamond [14],  $\text{MgF}_2$  [15], and the compound fluorides  $\text{KMgF}_3$  [16] and  $\text{YLiF}_4$  [17]. In the primal state these crystals are optically transparent. Under irradiation with high-energy electrons, neutrons,  $\gamma$ -rays, X-rays, or hard UV, or calcination in alkali metal vapor (additive coloration), anionic vacancies appear in the crystal lattice and serve to localize free electrons. The absorption bands of these (F) centers (vacancy + electron) give a typical coloring to the crystals.

The simplest of point defects is the anionic vacancy denoted in Fig. 1.1 by an open circle in place of an absent negative ion. The vacancy has an effective positive charge and capturing an electron, forms a defect whose electronic structure is similar to that of the hydrogen atom. Such an optical center is referred to as F-center and has absorption bands in the visible or UV spectral regions (for many reasons [10] F centers are not suitable for laser oscillation).

The other intrinsic electronic CCs on which oscillation has been obtained (see Fig. 1.1) are complexes derived from F centers. For instance, the  $\text{F}_2^+$  center consists of two neighboring anionic vacancies with one captured electron, the  $\text{F}_2$  center consists of two neighboring vacancies with two captured electrons (analog of the hydrogen molecule), and the  $\text{F}_2^-$  center is composed of a pair of vacancies with three captured electrons.

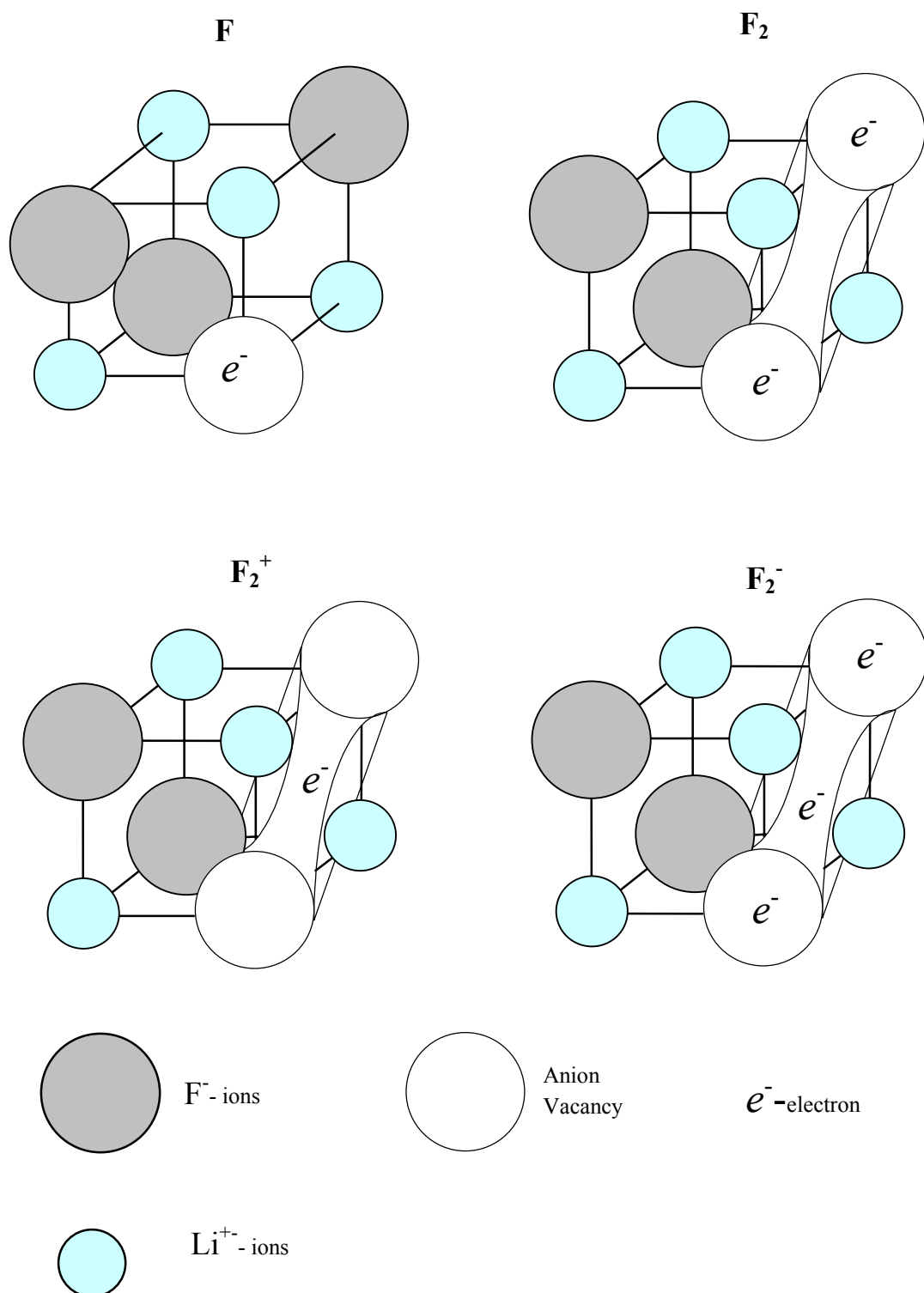


Fig. 1.1. Schematic drawings of the simple color centers in LiF crystal.

The principles of CCL operation can be accounted for using the Frank-Condon configuration diagram, which describes the optical properties of an electron system interacting with molecular or lattice vibrations: in particular, the optical transition of CCs. Pump radiation is absorbed in the wide band of the electric-dipole electron-vibrational transition  $1 \rightarrow 2$ . In a time on the order of  $10^{-12}$ - $10^{-13}$  s, radiationless relaxation to the minimum of potential curve of the excited electronic state,  $2 \rightarrow 3$  occurs, accompanied by a mutual rearrangement of the neighbouring ions and by phonon emission. Then a radiative electron-vibrational transition ( $3 \rightarrow 4$ ) occurs with a probability of  $A = 10^7$ - $10^8$  s<sup>-1</sup>, followed by another rapid vibrational relaxation ( $4 \rightarrow 1$ ) to the potential curve minimum of the ground electronic state with resetting of the spatial ion configuration. Disregarding the details, one may consider this scheme as the four-level laser scheme of oscillation.

### ***1.3. Color center formation in ionic crystals***

Color centers are formed in originally transparent crystals through ionic displacement caused by a high energy irradiation, or through creation of stoichiometric excess of alkali or alkali-earth metal in the crystal at elevated temperature. The latter method is called additive coloration and provides CC with higher stability.

The formation of aggregate CC in alkali halide crystals under ionizing radiation is a complicated process. It involves emergence, separation and subsequent association of primary Frenkel defects into the aggregate color centers as well as their recharging by electrons and band holes.

The necessary radiation damage can be produced by X-rays,  $\gamma$ -rays, neutrons, electrons or other charged particles. However, neutron beams are not readily available. The production of CC via electromagnetic field requires relatively long (days) exposure times but provides high homogeneity of CC.

The readily available electron beam is a commonly used irradiation source for CC preparation. To penetrate through the crystal with a thickness of several mm electrons with energies of 1-2 MeV are required and the crystal is usually exposed from both sides to provide sufficient homogeneity. The crystals are always irradiated at lower temperatures (77 – 177 K) with current density of about 10  $\mu\text{A}/\text{cm}^2$ . Irradiation time varies from several minutes to a few hours depending on the crystal lattice and the type of centers to be produced [9].

The procedure of additive coloration consists of calcination of the crystal in metal vapor at a temperature between the crystal melting point and the temperature of colloid formation.

For instance, for KCl the melting point is 768 °C, and the colloid formation is initiated at temperature 400 °C. As a result of this procedure, the alkali-metal atoms are captured and become ionized on the crystalline surface, attracting the halogen ions. The latter diffuse towards the surface, forming anion vacancies in the bulk of the crystal. The electrons appearing as a result of alkali metal atoms ionization also diffuse to be captured on the vacancies and form F centers. The crystal is then quickly cooled down to room temperature in order to avoid colloid formation. Further accumulation of the  $F_A$ ,  $F_B$ ,  $F_2^+$  centers is stimulated by additional light treatment of the crystal. The technology of alkali-halide crystals additive coloration was developed a long time ago. A detailed description of additive coloration technique and apparatus can be found in reference [18].

The technology of electrolytic coloration was also available rather a long time ago, but it was only in 1987, that the first laser crystals were produced using this technique [19]. The procedure runs as follows. A crystal is placed into a crucible and is heated to the temperature of anion mobility, at which "thermal" anion vacancies also appear. A direct current high-voltage electric field is applied to the crystal to drive an ionic current: anions move towards the anode and the cathode emits electrons. The latter are captured by the anion vacancies to form F centers. The next part of the crystal treatment, as in the case of additive coloration, involves fast crystal cooling and light treatment. The additive and electrolytic coloration techniques are better than radiational techniques because they produce more temperature- and light-resistant laser crystals. The disadvantages of the above-mentioned methods are the low coloring homogeneity, the poor optical quality of the crystals due to colloid formation, and the inability to produce large-size active media.

The formation of aggregate color centers in alkali-halide crystals under ionizing radiation is a complicated process. It involves emergence, separation, and recombination of primary Frenkel defects, association into aggregate  $F_2$ ,  $(F_2)_A$ ,  $F_2^+$ ,  $(F_2^+)_A$ ,  $F_2^-$ ,  $F_3$ ,  $F_3^+$ ,  $F_3^-$  and other color centers and recharging of color centers by electrons and band holes. The defect formation may run fast or slow. Decomposition of self-localized excitons into primary radiational defects and recharging of color centers are relatively fast processes ( $10^{-12}$  -  $10^{-7}$  s). Slow processes run either due to spatial diffusion of the defects and their associates, or due to diffusion of self-localized holes (resulting in color centers recharging).

All the above processes determine the efficiency of formation of any type of color centers. These processes depend upon the temperature of irradiation and storage of the crystal,

impurity composition of the initial material, ionizing radiation dose power and irradiation dose.

Separated electrons and holes, free and self-localized excitons are generated in alkali-halide crystals under ionizing irradiation. Self-localized excitons decompose with the emergence of pairs of F-centers and interstitial halogen atoms (H). A fast recharging of these pairs under flux of electrons gives rise to actually simultaneous formation of the anion vacancies  $V_a^+$  and interstitial halogen ions  $I_a^-$  [20]:



The mechanisms of formation of aggregate centers through migration of anion vacancies have been studied by Delbecq [21]. According to this paper, charged  $F_2^+$  centers first appear, and then capture electrons to produce neutral  $F_2$  centers:



Simultaneously with a fast process of electron capture,  $F_2^+$  centers may take part in a slow temperature-dependent migration process. Colliding with the F,  $F_2^+$  and  $F_2^-$  CCs, they form more complex CCs -  $F_3^+$ ,  $F_4^+$ , and  $F_4$ , respectively:



whose further aggregation leads to the appearance of colloid particles in the crystal. The processes of  $F_2$  CCs formation by scheme (3.4) are competing with the processes of their ionization due to a fast capture of free electrons:



or holes



or due to diffusion processes involving mobile anion vacancies



and self-localized holes



These processes (4,8,9,11) leading to recharging in the group of  $F_2$ ,  $F_2^+$ , and  $F_2^-$  CCs, are also inherent in the group of  $F_3$ ,  $F_3^+$ , and  $F_3^-$  CCs.

The ratio of the contributions of different reactions depends on the irradiation procedure and impurity composition in the irradiated crystal. The optimization of irradiation treatment to create  $F_2^-$  and  $F_2^+$  stabilized color centers in doped LiF crystals is discussed below.

#### ***1.4. LiF:F<sub>2</sub><sup>-</sup> active element optimization***

Below we use for example the LiF crystal with  $F_2^-$  CC to illustrate the directions of irradiation parameters optimization which have permitted to overcome the technological difficulties faced when producing an optically dense active medium.

The LiF:F<sub>2</sub><sup>-</sup> crystals combining unique modulation, thermal, and operational characteristics, are now widely used as active media in tunable lasers and as nonlinear elements with saturable absorption for neodymium laser Q-switches. However, available techniques of such laser crystals preparation fail to produce optically dense, high-contrast media required for a series of applications. Usually, the value of active absorption at the working wavelength does not exceed 0.4-0.6 cm<sup>-1</sup> at a contrast (ratio of the active absorption coefficient to the loss coefficient at  $\lambda = 1.06 \mu\text{m}$ ) of 10-20. Under the action of  $\gamma$ -quanta commonly used for producing LiF:F<sub>2</sub><sup>-</sup> laser crystals, the  $F_2^+$  CCs emerging by reaction (3) may be involved in three processes: a) fast process of electron capture to produce  $F_2$  CCs (reaction 4) and  $F_2^-$  CCs (reaction 8); b) slow diffusion processes of aggregation of the type 5, 6, 7; c) dissociation on the F center and anion vacancy  $F_2^+ \Rightarrow F + V_a^+$ .

The rates of the processes and final concentration of CCs depend, as was already mentioned, on the impurity composition of the initial material, irradiation dose, power, and crystal temperature. Varying the ratio of these parameters, one can essentially influence the processes of  $F_2^-$  CC formation in LiF.

When we optimized the procedure of LiF crystal treatment under ionizing irradiation so, that the processes 3, 4 were efficient and 5-7 – negligible, maximum active absorption of  $F_2^-$  CCs at the wavelength 1.064  $\mu\text{m}$  exceed 1.5 cm<sup>-1</sup> at a contrast as high as 20 – 40.

Optimization of the pumping wavelength is essential parameter limiting the oscillation efficiency. For example in  $F_2^-$  CC in LiF (LiF:F<sub>2</sub><sup>-</sup>) absorption spectra overlaps with neodymium pump sources. Besides due to small Stokes shift absorption band overlaps with luminescence band. As a result the main generation parameters of LiF:F<sub>2</sub><sup>-</sup> lasers (such as tunable range, efficiency) depend on optimization of pump laser. The aim of the work was the

development of active elements on the base of  $\text{LiF:F}_2^-$  and  $\text{NaF:F}_3^-$  crystals and optimization of their parameters to develop the high-efficient  $\text{LiF:F}_2^-$  and  $\text{NaF:F}_3^-$  CC lasers.

During the  $\text{LiF:F}_2^-$  crystal technological preparation the special attention should be paid to the presence of the aggregate color centers with absorption in the oscillation spectral range. We carried out special experiments to test  $\text{LiF:F}_2^-$  active elements developed under different irradiation conditions and prepared from the samples of bulk crystals provided by different suppliers. The absorption coefficients of  $\text{LiF:F}_2^-$  samples in the maximum of  $\text{F}_2^-$  color centers absorption band (940 nm), pump wavelength (1064 and 1047 nm) and parasitic losses due to the presence of highly aggregated parasitic centers (typically measured at 1300 nm) were controlled. The laser oscillation efficiency of these active elements was studied in non-selective flat-flat mirrors cavity. Quasi-longitudinal pumping was carried out by the radiation of the fundamental frequency of Q-switched  $\text{YAG:Nd}^{3+}$  laser with pulse duration  $t_p=30$  ns and pulse repetition rate 12 Hz. The diameter of the pumping beam in front of the  $\text{LiF:F}_2^-$  crystal was 3 mm. The  $\text{LiF:F}_2^-$  active element (40mm long) was set at Brewster angle to the cavity axis.

The  $\text{LiF:F}_2^-$  oscillation efficiency dependence on pump energy is presented in Fig. 1.2. As one can see at low pump energy the increase of the output mirror reflection from  $R=12\%$  to  $R=35\%$  leads to the increasing of the laser efficiency in 1.5 times (from 37% to 45%). In the case of high pump energy a mirror with reflection coefficient  $R=20\%$  is optimal. In this case laser efficiency for different output coupler are close to each other. Maximum  $\text{LiF:F}_2^-$  laser efficiency was achieved with  $R=20\%$  output coupler and pump energy 70 mJ and was equal to  $\eta=56\%$ . It corresponds to the 70% of quantum efficiency with respect to absorbed energy.

As it was written above the overlapping of the absorption and emission bands of the  $\text{F}_2^-$  CC at the pumping wavelength limit the maximum of active media amplification. The saturation in the active media under pumping will be obtained when the stimulated absorption rate is equal to the stimulated emission induced by the pump radiation. The value of the maximal inversion of the active media can be obtained from the following equation :

$$N_2^{sat}(\nu_p) = \frac{N\sigma_{12}(\nu_p)}{\sigma_{21}(\nu_p) + \sigma_{12}(\nu_p)}$$

where  $N$  is full  $\text{F}_2^-$  CC concentration,  $\sigma_{12}(\nu_p)$ ,  $\sigma_{21}(\nu_p)$ - absorption and emission cross section at pumping wavelength,  $N_2^{sat}$ - maximum of the inversion density in the active media. Using absorption and emission spectra we can calculate and compare the saturated inversion and



laser gain under different pumping wavelength. Fig. 1.3 shows the effective partial concentration of excited CC versus pumping wavelength. As one can see under YAP:Nd<sup>3+</sup> laser ( $\lambda=1.079 \mu\text{m}$ ) radiation we can excite only 16% of whole concentration of active color centers. For YAG:Nd<sup>3+</sup> ( $\lambda=1.064 \mu\text{m}$ ) and YLF:Nd<sup>3+</sup> ( $\lambda=1.047 \mu\text{m}$ ) laser radiation this value can be increased up to 26% and 43% correspondingly. So the small shift of the pumping radiation wavelength from  $1.079 \mu\text{m}$  to  $1.047 \mu\text{m}$  leads to the increasing of the excited CC concentration and laser gain in 2.7 times. For one of the shortest pump wavelength ( $\lambda = 1.041 \mu\text{m}$ ) which corresponds to LaF<sub>3</sub>:Nd<sup>3+</sup> laser more than 3 times improvement can be predicted. In our experiments we investigated tunable LiF:F<sub>2</sub><sup>-</sup> laser oscillation under pumping with commercial YAG:Nd<sup>3+</sup> and YLF:Nd<sup>3+</sup> lasers and specially developed laser with LaF<sub>3</sub>:Nd<sup>3+</sup> active element.

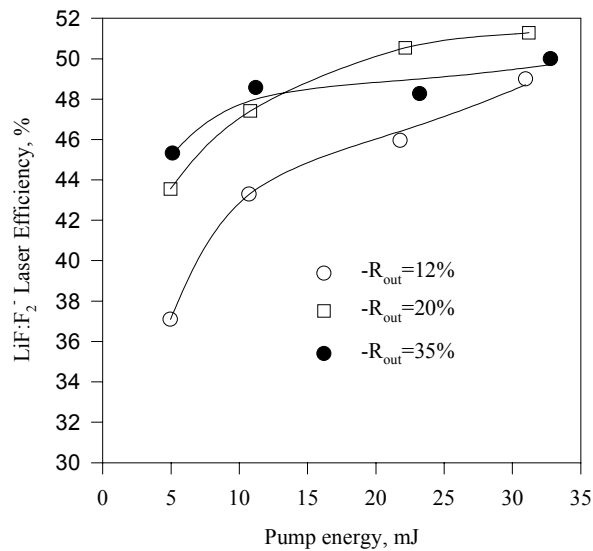


Fig. 1.2. LiF:F<sub>2</sub><sup>-</sup> laser efficiency versus pump energy in non selective flat-flat cavity for different output coupler reflectivity R<sub>out</sub>

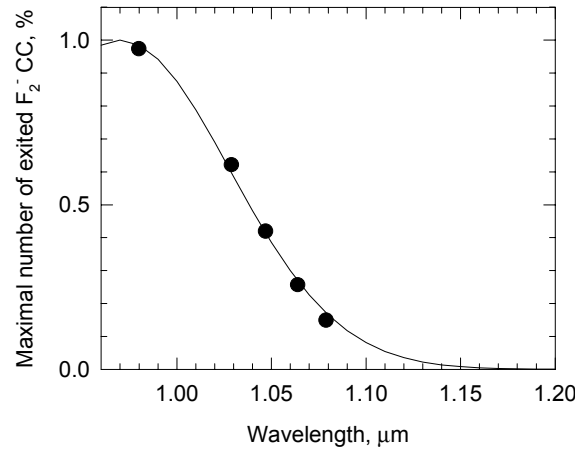


Fig. 1.3. Maximal of exited state concentration of  $F_2^-$  color center in LiF crystal under different pumping wavelengths 0.98  $\mu\text{m}$  (InGaAs), 1.041  $\mu\text{m}$  ( $\text{Nd}^{3+}:\text{LaF}_3$ ), 1.047  $\mu\text{m}$  ( $\text{Nd}^{3+}:\text{YLiF}_4$ ), 1.064  $\mu\text{m}$  ( $\text{Nd}^{3+}:\text{YAG}$ ) 1.078  $\mu\text{m}$  ( $\text{Nd}^{3+}:\text{YAP}$ ).

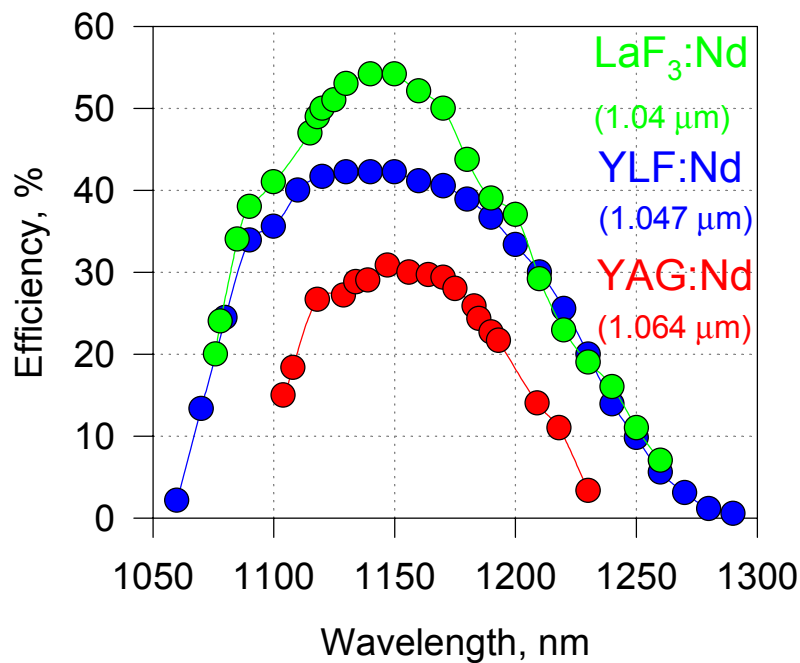


Fig. 1.4. Tuning curve of LiF: $F_2^-$  Color Center Laser pumped with  $\text{YAG}:\text{Nd}^{3+}$ ,  $\text{YLF}:\text{Nd}^{3+}$  and  $\text{LaF}_3:\text{Nd}^{3+}$  lasers.

We studied LiF: $F_2^-$  laser oscillation parameters in a selective cavity formed by flat dichroic input mirror and diffraction grating operating in autocollimation regime. In the

spectral range 1.07-1.3  $\mu\text{m}$  the input dichroic mirror had high reflectivity close to 100% and transmission at pumping wavelength equaled to 85%. The efficiency of the diffraction grating (1200 grooves/mm) in autocollimation regime was about 20% and zero diffraction order was used as output coupler. The  $\text{LiF:F}_2^-$  active element was 8 cm long and had polished faces cut at Brewster angle. The pump sources were  $\text{YAG:Nd}^{3+}$ ,  $\text{YLF:Nd}^{3+}$  and  $\text{LaF}_3\text{:Nd}^{3+}$  Q-switched laser. Fig. 1.4 shows tuning curves of  $\text{LiF:F}_2^-$  color center laser under different pumping. In all cases pump energy was about 30 mJ. One can see from the figure that the efficiency of the  $\text{LiF:F}_2^-$  laser oscillation in the maximum of the tuning curve was 22%, 39% and 50% for  $\text{YAG:Nd}^{3+}$ ,  $\text{YLiF}_4\text{:Nd}^{3+}$  and  $\text{LaF}_3\text{:Nd}^{3+}$  pump sources, correspondingly. Besides this the tuning range was extended up to 1.064-1.29  $\mu\text{m}$  for  $\text{YLiF}_4\text{:Nd}^{3+}$  and  $\text{LaF}_3\text{:Nd}^{3+}$  pump lasers in comparison to 1.09 ÷ 1.25  $\mu\text{m}$  for  $\text{YAG:Nd}^{3+}$  pump.

#### 4.2. NaF color center crystal optical and laser characteristics

Three types of sodium fluoride color center crystals which differ both in the impurity doping composition, growth and irradiation conditions were developed and purchased. Fig. 1.5 presents the absorption spectra of the above mentioned crystals, as well as those of a nominally pure NaF crystal (curve 4) recorded at 300 K and their spectra of luminescence. From Fig. 1.5 one can see that the spectra of these crystals strongly differ in the intensity of the absorption bands and the spectral position of their maxima. Nominally pure NaF crystals are characterized by weaker absorption as compared to the doped NaF crystals. Also the pure crystals have no absorption bands with maximum in a range of 0.8-0.9  $\mu\text{m}$  or luminescence with excitation by 1.06  $\mu\text{m}$  radiation. The NaF crystals of all three types, which have an identical absorption coefficient at a wavelength of 1.06  $\mu\text{m}$ , are characterized by different color center composition.

For instance, the spectrum of luminescence of type 2 crystals has a maximum of 1.16  $\mu\text{m}$  and a half-width equals 1560  $\text{cm}^{-1}$ . The spectrum of the type 1 crystal is shifted with respect, to the spectrum of the type 2 crystals by 150  $\text{cm}^{-1}$  to the longer wavelength region ( $\lambda_{\text{max}}=1.18 \mu\text{m}$ ) with a half-width equaled to 1700  $\text{cm}^{-1}$ . The luminescence spectrum of type 3 crystal is further shifted to the infrared region and consists of at least two bands with maxima at 1.28 and 1.44  $\mu\text{m}$ . The obtained results indicate that the examined three types of NaF crystals are of interest as active laser elements in a range of 1.1-1.5  $\mu\text{m}$ . To estimate the perceptiveness of the examined crystals as laser active mediums, the experiments on the

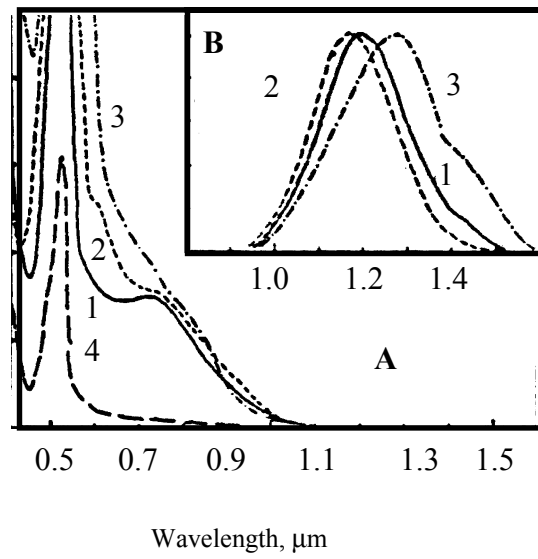


Fig. 1.5. Absorption spectra (A) luminescence spectra (B) of NaF crystals.

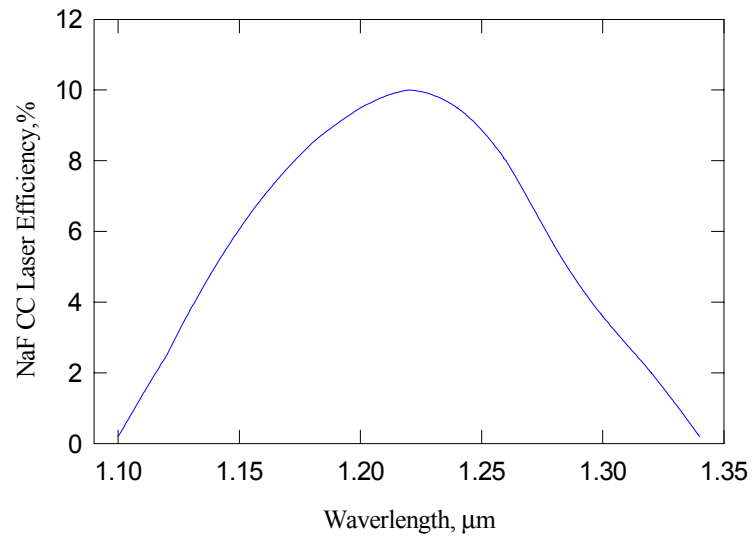


Fig. 1.6. Tuning Curve of NaF Color Center Laser.

investigation of their absorption saturation under the pumping with unfocused radiation at wavelength of 1.06  $\mu\text{m}$  were performed. It turned out that all three types of NaF crystals exhibit the saturation of absorption and can operate as passive Q-switches for neodymium

laser up to a pumping energy density of  $0.4 \text{ J/cm}^2$ . But crystals of the 1 and 2 type are not bleached under  $10^5$  pumping pulses with an energy density of  $0.4 \text{ J/cm}^2$ , pulse duration of 15 ns and 12.5 Hz repetition rate. While the CC concentration and absorption in type 3 crystals was reduced three times after 10 minutes of  $1.06\text{-}\mu\text{m}$  pump irradiation. Therefore, further generation tests were performed only for type 1 and 2 NaF crystals.

Broad band oscillation at  $\lambda = 1.25 \text{ }\mu\text{m}$  and a half-width  $\Delta\nu = 100 \text{ cm}^{-1}$  was realized in a nonselective resonator with flat high reflection mirrors ( $R=100$ ,  $R_{\text{out}}=95\%$ ) under longitudinal pumping by  $1.064 \text{ }\mu\text{m}$  radiation. As active elements we used 2 cm long NaF:Li(OH) crystal with absorption  $K=0.35 \text{ cm}^{-1}$  at pumping  $1.064 \text{ }\mu\text{m}$  wavelength. The laser efficiency was 7.5%, slop efficiency was 13% and the oscillation threshold was  $15 \text{ mJ/cm}^2$ .

Testing the NaF with color centers under two different wavelength of pumping  $1.064\text{ }\mu\text{m}$  (Nd:YAG) and  $1.047\text{ }\mu\text{m}$  (Nd:YLF laser) shows 3 times increase of the output energy and efficiency for Nd:YLF laser. This is due to the increase of the amplification gain and is in a very good agreement with oscillating results of LiF:F<sub>2</sub><sup>-</sup> color center laser.

The tunable oscillation of 2 type 8 cm NaF crystal was studied in the same selective cavity as LiF:F<sub>2</sub><sup>-</sup> laser. The maximal oscillation energy was 10 mJ at 100 mJ pumping energy and pulse repetition rate -7 Hz. The tuning curve of NaF CC laser is shown in Fig. 1.6. From Fig. one can see that the oscillation was obtained in  $1.1\text{-}1.34 \text{ }\mu\text{m}$  spectral range. The maximum laser efficiency equaled to 10%. There was no any degradation of laser efficiency during three day operation at room temperature. Three month storage of the active element at room temperature led to a noticeable reduction of the laser parameters. But it should be noted that the thermostability of active elements of the type 2 NaF may be increased by several times under low temperature ( $T < 0^\circ\text{C}$ ) storage in the refrigerator between operational cycles.

Fig. 1.7 presents the investigated samples of LiF:F<sub>2</sub><sup>-</sup> and NaF color center crystals.

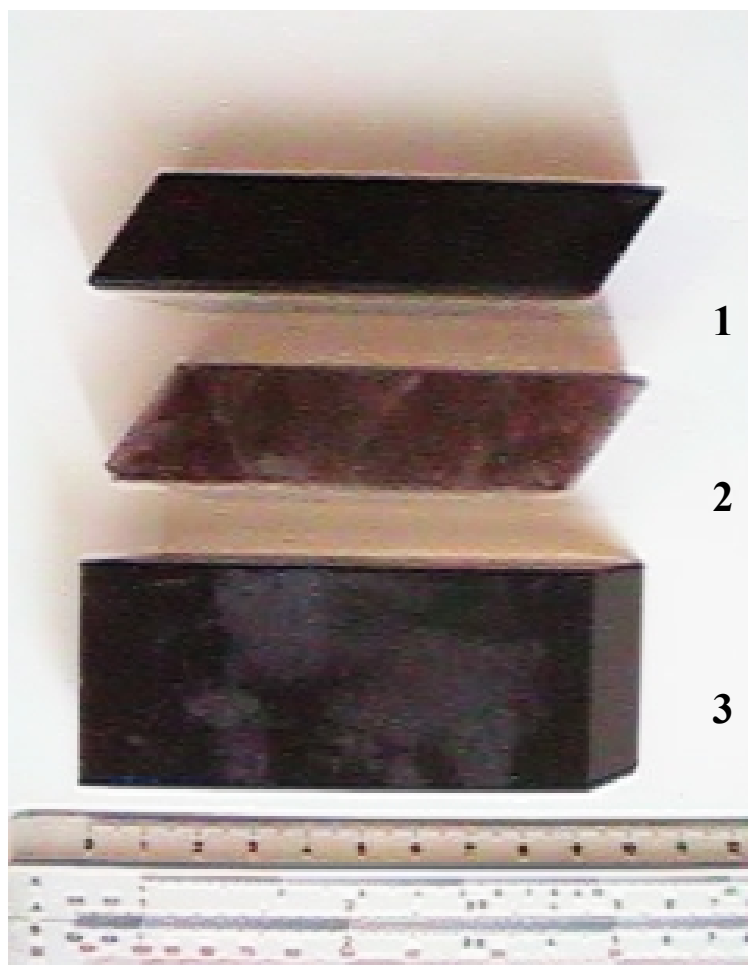


Fig. 1.7. The investigated samples of color center crystals  
 $\text{LiF:F}_2^-$  (1,3) and  $\text{NaF}$  (2).

## 2. Optical scheme of color center oscillator

As it was shown above the efficiency of  $\text{LiF:F}_2^-$  CCL is increased when using the pump source with shorter wavelength instead of usual  $\text{Nd}^{3+}:\text{YAG}$  laser. The most perspective and available pump source is pulsed nanosecond  $\text{Nd}^{3+}:\text{YLiF}_4$  with 1047 nm oscillating wavelength. The laser developed in our lab has an oscillator and the amplifier stages. It provided pulses with 200 mJ energy, 12 ns pulse duration at 3 pps repetition rate with smooth spatial distribution.

To obtain the required spectral parameters of tunable laser one should use Master Oscillator and Power Amplifier (MOPA) scheme. In this case the oscillator provides rather weak laser pulses with narrow linewidth and smooth spatial profile. These pulses are amplified to the required energy value. The principal scheme of such laser system is presented in Fig. 2.1. The pump beam was split into two with energy ratio 1/5. Most part of the beam excites  $\text{LiF:F}_2^-$  color center powerful amplifier. Another part is used to pump  $\text{LiF:F}_2^-$  narrow line color center oscillator.

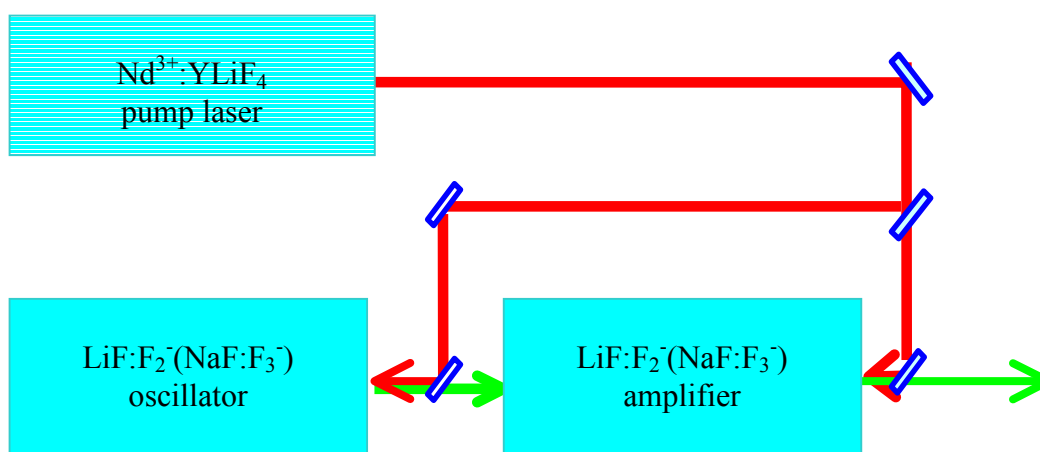


Fig. 2.1. Principal scheme of the experimental setup for powerful narrow line CCL with  $\text{Nd}^{3+}:\text{YLiF}_4$  pump laser.

The optical scheme of the optimized narrow line color center laser oscillator is shown in Fig. 2.2. It includes high reflectivity diffraction grating, Fabri Perrot etalon, intracavity prism telescope, intracavity 45° dichroic mirror, Brewster cut active element and output coupler. Such design protects diffraction grating from high pump power and allows good spatial overlapping of pump and oscillating beams. The pump beam is delivered by

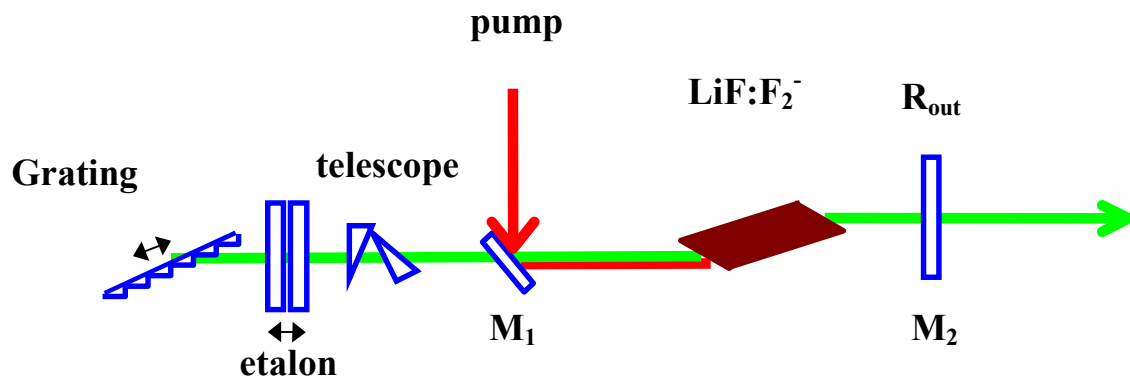


Fig. 2.2. Tunable LiF:F<sub>2</sub><sup>-</sup> color center laser oscillator.

prism or HR mirror to the oscillator unit. The laser unit can be optionally added with prism telescope. The principle of laser oscillation is as following. Neodymium laser pump beam with horizontal polarization is reflected by the intracavity dichroic selective mirror M<sub>1</sub>. It has high reflectivity at 1.04-1.06  $\mu\text{m}$  wavelength under 45° incidence angle and low reflectivity for oscillating wavelengths. The pump beam is absorbed in the Brewster LiF:F<sub>2</sub><sup>-</sup> active crystal. The pump radiation excites the oscillating F<sub>2</sub><sup>-</sup> color centers. The laser cavity with positive feedback arranges the conditions for oscillation of  $1.06 \div 1.29 \mu\text{m}$  radiation. The diffraction grating and Fabri Perrot etalon are used for spectral dispersion. Diffraction grating works in the autocollimation regime, so that the first order of diffraction is reflected back into the cavity. The diffraction angle determines the oscillating wavelength. Rotation of the grating allows wavelength tuning. Solid state Fabri Perrot etalon is a glass or quartz plane-parallel plate with mirror coatings on both surfaces. It can be tuned by its rotation around the axis. The intracavity prism telescope extends the beam incident to the grating and increases spectral selectivity of the cavity. The output coupler provides the positive feedback for the laser cavity. Below specific features of each optical element are discussed and their real characteristics are presented.



The real implementation of the laser unit is shown in Fig. 2.3 and 2.4. Diffraction grating (1) is installed on the rotating stage. Fabri Perrot etalon (2) has a special mounting. Intracavity prism telescope (3) and 45-degrees dichroic mirror (4) are located close to the active element (5) mounted together with transparent active element simulator for adjustment. The output coupler (6) ends the cavity from the right hand side. Mirror (7) is used to deliver pump beam to the cavity.

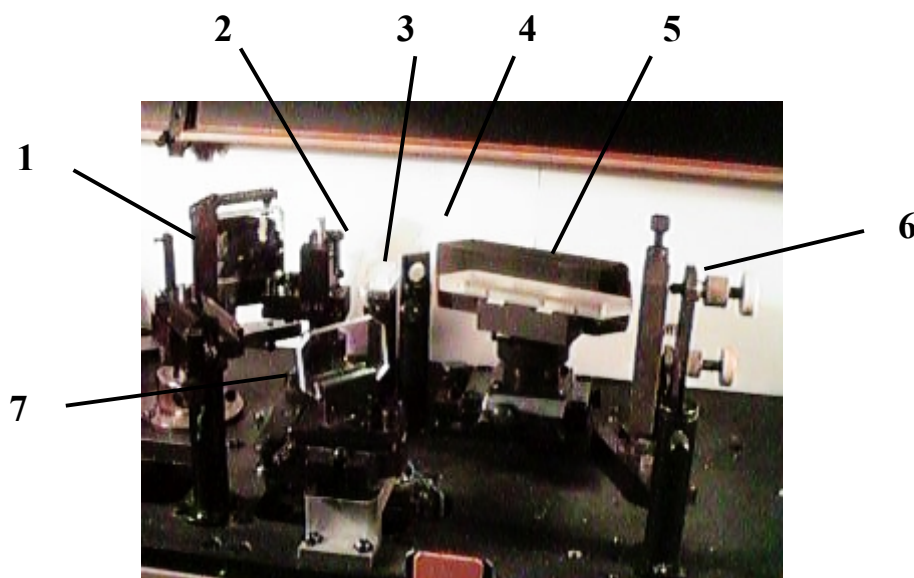


Fig.2.3. The narrow line laser cavity components.

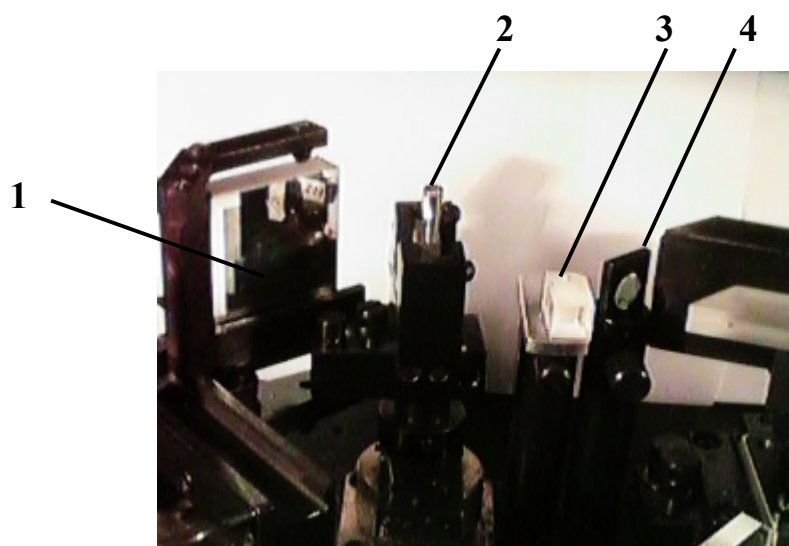


Fig. 2.4. Dispersive elements of the narrow line laser.

### 2.1. $\text{LiF:F}_2^-$ color center active element

The laser operation principle is based on the effect of lasing of alkali-halide crystals LiF with  $\text{F}_2^-$  color centers when they are excited by the pumping laser radiation. Laser active elements are prepared from the irradiated lithium fluoride crystals. Working color centers are intrinsic defects of crystal lattice - two neighboring anion vacancies localized three electrons -  $\text{F}_2^-$  color centers. These objects are thermally stable at room temperature with stability more than 10 years at 300 K.  $\text{F}_2^-$  color centers can effectively absorb and emit photons with quantum yield about 60%. They have wide absorption and luminescence bands with maxima 0.96 and 1.12  $\mu\text{m}$ , half-width 1700 and 1400  $\text{cm}^{-1}$ , respectively. They have high values of oscillation strength of electron-vibrational transitions, short radiation lifetime - 55 ns, large Stokes shift of luminescence to obtain oscillation at 300 K according to quasi four level scheme. The wavelength of radiation of widely spread neodymium lasers gets into the absorption band of  $\text{F}_2^-$  color centers that allows to make tunable in near IR high efficient lasers pumped by fundamental harmonic of neodymium nanosecond pulsed  $\text{Nd}^{3+}:\text{YAG}$  laser or other neodymium lasers with host material like: GGG, GSGG,  $\text{YLiF}_4$ ,  $\text{LaF}_3$ , glass etc.

The use of the active element with Brewster cut faces allows to solve the following problems:

- ⇒ minimize the reflection losses for the pump radiation;
- ⇒ minimize the reflection losses for the lasing radiation;
- ⇒ keep the certain polarization direction of the output laser radiation.

The refraction index of LiF crystal is 1.38. This means that the incident Brewster angle equals to  $54^\circ 50'$ . The angular dependence of the reflection from the crystal face is described by the Fresnel equations.

$$R_{\parallel} = \left( \frac{\text{tg}(\theta_1 - \theta_2)}{\text{tg}(\theta_1 + \theta_2)} \right)^2$$

$$R_{\perp} = \left( \frac{\sin(\theta_1 - \theta_2)}{\sin(\theta_1 + \theta_2)} \right)^2$$

We are interested in the reflectivity of the radiation with polarization parallel to the incident plane  $R_{\parallel}$ . It is equal to zero when  $\theta_1 + \theta_2 = \pi/2$ , that is known as Brewster angle. Fig. 2.5 presents the dependence of the reflectivity  $R_{\parallel}$  versus incident angle at LiF crystal

face. One can see that the accuracy of the angular alignment of the crystal face is not very critical. The reflection is less than 0.2% for incident angle of  $53^\circ \div 55^\circ$ .

The draught of LiF color center active elements with 80 mm length is shown in Fig. 2.6. The use of active element with Brewster cut windows result in the slight increase of the cavity length. For 20 mm thick crystal this results in 14.5 mm increase. This should be taken into account when designing compact laser cavity. Fig. 2.7 presents the picture of irradiated LiF color center crystals.

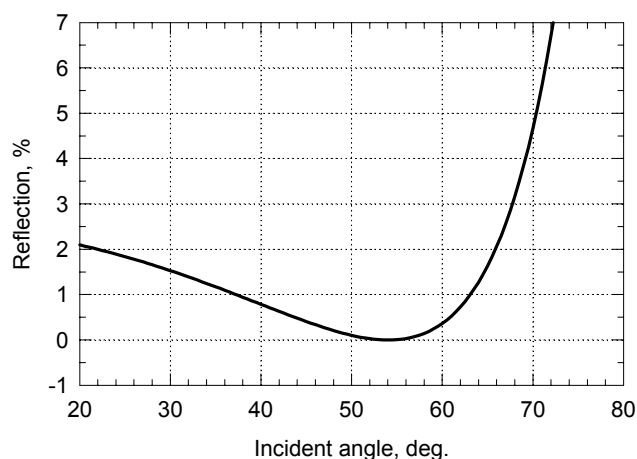


Fig. 2.5. The reflectivity of the radiation with polarization parallel to the incident plane  $R_{//}$  versus the incident angle at LiF crystal face.

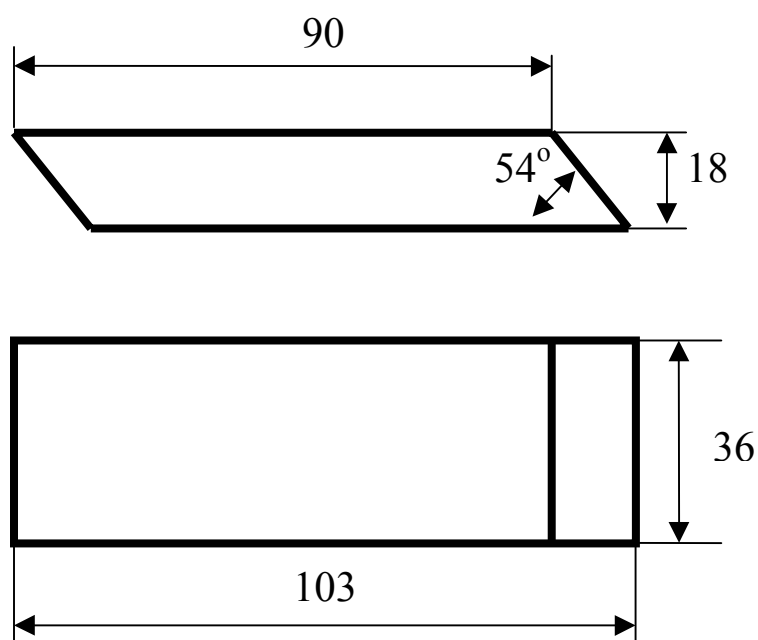


Fig. 2.6. Drawing of LiF color center crystal with Brewster cut faces 90 mm long.

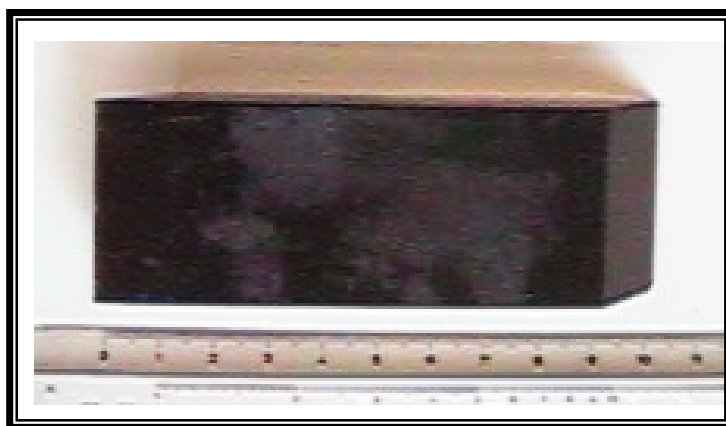


Fig. 2.7. Picture of irradiated LiF color center crystal active element  
with Brewster cut faces 90 mm long.

## 2.2. Dichroic intracavity mirror

The dichroic has high reflectivity at 1.03-1.06  $\mu\text{m}$  wavelength with  $45^\circ$  incidence angle. It has low reflectivity at the oscillating wavelength from 1.08 to 1.30  $\mu\text{m}$  wavelength. Fig. 2.8 presents the reflectivity spectrum of the working surface of mirror  $M_1$  used in experiments. The reflectivity was about 4% for 1.04-1.06  $\mu\text{m}$  spectral region and more than 90% for 1.12-1.3  $\mu\text{m}$ . Another surface had antireflection coating (Fig. 2.9).

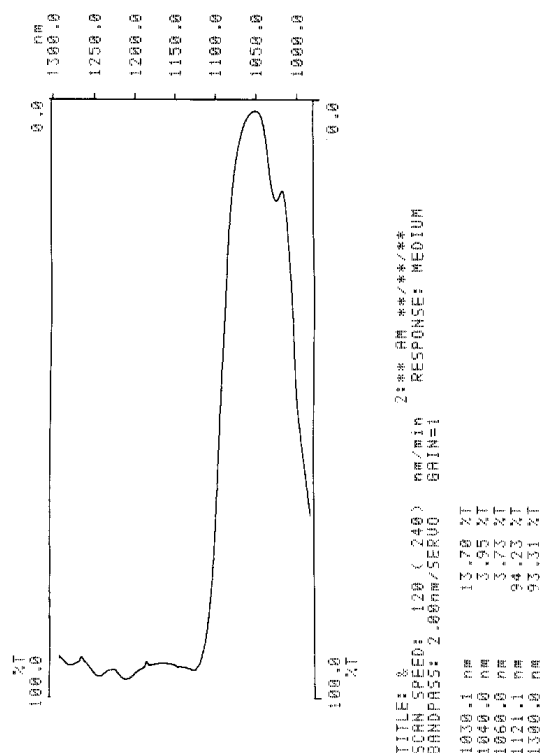


Fig. 2.8. The reflectivity of the working surface of mirror  $M_1$  with  $45^\circ$  incidence angle.

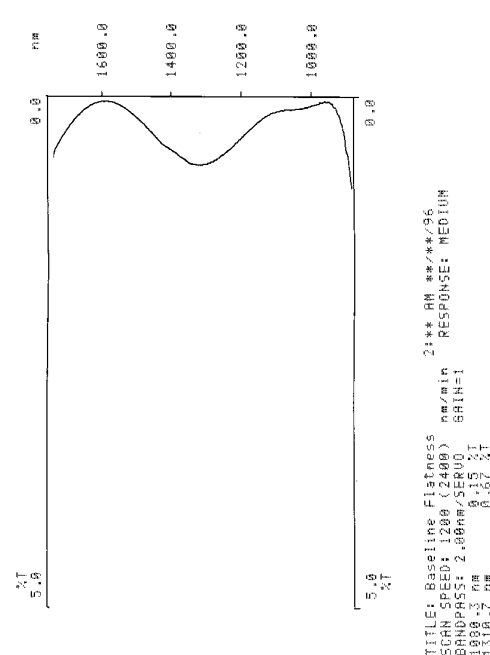


Fig. 2.9. Zero reflection of the second surface of mirror  $M_1$  with  $45^\circ$  incidence angle.

### 2.3. Diffraction grating

Diffraction grating is the main selective element in the tunable  $\text{LiF:F}_2^-$  CCL. The investigation of its properties is very important in designing optimal cavity configuration. Typical reflection diffraction grating used in the tunable CCL is metal and characterized by 1200 lines per mm. This allows them to work in the auto-collimating scheme from 840 to 1270 nm in the first order of diffraction. The higher spectral resolution requires special development of diffraction gratings with large reflectivity at grazing incidence angles. The main drawback of metal grating is that they have absorption in a thin metal layer. This is very important especially for high power lasers due to high heating resulting in their damage. This is a reason why holographic gratings with autocollimation reflection of light from the surface of corrugated waveguides with the leaky modes were investigated in this project.

Below we present the results on investigation the diffraction properties of the waveguide-grating structure with the least possible number of dielectric layers and on the search of the conditions when 100% diffraction efficiency of the grating can be achieved with the minimal depth of the corrugated structure.

#### *Analysis of Diffraction Properties of a Single-Layer Corrugated Structure*

A schematic diagram of a simplest waveguide with leaky modes is shown in Fig. 2.10. Contrary to an ordinary waveguide with a layer that has higher refractive index than that of the substrate ( $n_f > n_s$ ), the dielectric layer of the investigated waveguide possesses  $n_f < n_s$ . The modes of such waveguide undergo a total reflection at the boundary of layer with air and only partial reflection at its interface with a substrate.

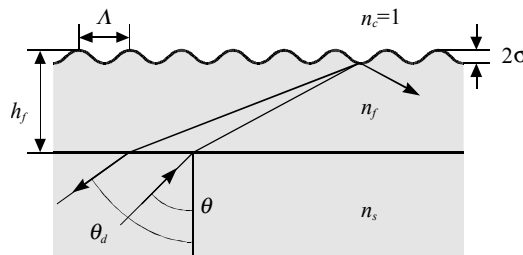


Fig. 2.10. Scheme of a single-layer corrugated structure.

The equality of the phase change of the wave traveling from one layer boundary to the other and back to the value  $2\pi m$  determines the condition of the leaky-mode existence in the dielectric layer under consideration. In fact this condition corresponds to the excitation of the waveguide mode, which interacts with the grating until the complete escape from the waveguide. We used the program for personal computer written on the basis of the method of “sources” to calculate the grating depth, which results in 100% autocollimation reflectivity. This program allows one to calculate the parameters of various corrugated structures at considerable depths of the grating. As an example, we considered  $\text{MgF}_2$  layer ( $n_f=1.383$ ) at  $\text{SiO}_2$  substrate ( $n_s=1.458$ ) and the corrugation period  $\Lambda=0.273\mu\text{m}$  with the optimal depth value of the grating  $2\sigma=0.36\mu\text{m}$  providing the layer thickness  $h_f=0.43\mu\text{m}$ . The light beam with a wavelength  $\lambda=633\text{ nm}$  was incident from the substrate at an angle  $\Theta=52.6^\circ$ . With a small value of grating period, the manufacturing of the grating with such considerable depth becomes difficult. Due to this we decided to consider the corrugated waveguide structures with higher interaction length of the mode with the grating.

#### *Analysis of Diffraction Properties of a Double-Layer Corrugated Structure*

The schematic diagram of the investigated structure is presented in Fig. 2.11. One of the layers of this structure is the buffer with a refractive index  $n_b < n_f$  while the other layer is the waveguide one with  $n_f < n_s$ .

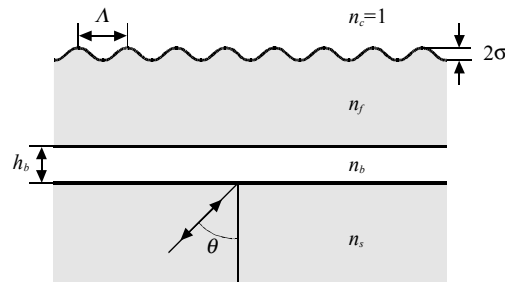


Fig. 2.11. Scheme of a double-layer corrugated structure.

Two types of the leaky modes are possible in this structure. First of them is characterized by higher refractive index of the mode  $n^*$ , i.e.,  $n_b < n^* < n_f$ , and  $l < n^* < n_b$  for the second one. Both types of modes undergo total internal reflection at the air/dielectric layer interface. At the dielectric layer/substrate interface, the leaky modes of the first type undergo broken total reflection while the modes of the second type experience an ordinary Fresnel reflection.

Let us consider initially the autocollimation reflection of light with the participation of the leaky modes with  $n_b < n^* < n_f$ . Fig. 2.12 shows the dependencies of  $R_{-1}(h_b)$  on the thickness of the buffer layer for three different depths of the grating:  $2\sigma = 100, 50$ , and  $25$  nm. The calculations were performed for the structure with the following parameters:  $n_f = n_s = 1.458$  ( $\text{SiO}_2$ ),  $n_b = 1.383$  ( $\text{MgF}_2$ ),  $\Lambda = 0.2227 \mu\text{m}$ ,  $\lambda = 0.633 \mu\text{m}$ ,  $n^* = 1.42$ ,  $h_f = 0.675 \mu\text{m}$ , and  $\Theta = 77$  degrees. The corrugation was assumed to be sinusoidal in the calculations. As illustrated in Fig. 2.12, the smaller the depth of the grating, the higher the thickness of the buffer layer with which  $R_{-1} = 100\%$  is achieved.

Fig. 2.13 presents the angular dependencies  $R_{-1}(\Theta)$  for the same structure but for various depths of the grating. The behavior of the spectral dependencies of  $R_{-1}$  is similar.

Let's consider now the leaky modes with  $1 < n^* < n_b$ . As already mentioned above, they are characterized by the lack of the total internal reflection at the plane boundary of the waveguide (see Fig. 2.11). The Q-factor of these modes varies periodically with the increase

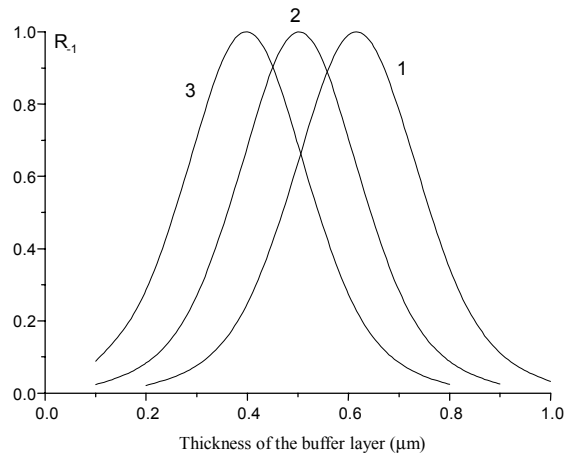


Fig. 2.12. Dependence of  $R_{-1}(h_b)$  on the thickness of the buffer layer for three different depths of the grating structure:  $2\sigma = 100$  (curve 1),  $50$  (curve 2), and  $25$  nm (curve 3).



in the thickness of the buffer layer, which results in different dependencies of  $R_{-1}$  on  $h_b$  with the excitation of these leaky modes. The considerably lower diffraction efficiency of the grating in the case being considered here is determined by the small Q-factor of the leaky modes with  $l < n^* < n_b$ , i.e., by the small path length of them in the corrugated layer. The increase in the path length of these modes can be achieved in the structure with larger number of layers shown in Fig. 2.14.

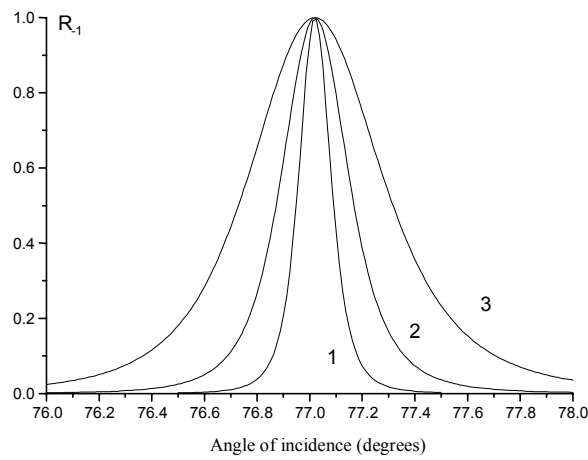


Fig. 2.13. The angular dependencies  $R_{-1}(\theta)$  for the same structure but for various depths of the grating.  $2\sigma=100$  (curve 1),  $50$  (curve 2), and  $25\text{ nm}$  (curve 3).

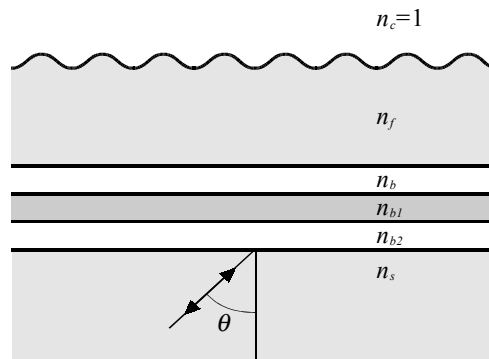


Fig. 2.14. The drawing of the discussed structure with two additional buffer layers and 99.2% reflectivity.

The thicknesses of two additional buffer layers in this structure are chosen from the condition:

$$h_b = \lambda / (4 \cdot n_b \cdot \cos \Theta_b)$$

i.e., from that of the constructive interference of the beams, which are reflected from the layers and form the waveguide mode. This interference increases the reflectivity of light and leads to the increase in the Q-factor of a mode.

The calculations of the autocollimation reflection show that the reflectivity  $R_1$  of the discussed structure (see Fig. 2.14) reaches of 99.2% at  $2\sigma = 50 \text{ nm}$ . However, if we confine ourselves to only one additional buffer layer with  $n_{b1} = 2.1$ , we obtain in this case only  $R_1 = 82\%$  with the same depth of the grating. This is 10 times that of the structure with one buffer layer and  $n_b = 1.383$ . Thus the increase in Q-factor of a mode of the corrugated structure allows one to enhance the efficiency of the diffraction of light in this structure.

#### *Spectral and Angular Dependencies of Autocollimation Reflection of Light at $1 < n^* < n_b$*

We have studied in detail a corrugated layer structure with  $n^*$  in the range  $1 < n^* < n_b$ . The schematic diagram of this structure is shown in Fig. 2.14. The following parameters of the structure were used in the calculations:  $n_f = 1.458$ ,  $n_b = 1.383$ ,  $n_{b1} = 2.05$ ,  $n_s = 1.512$ ,  $h_f = 0.37 \mu\text{m}$ ,  $h_b = 0.164 \mu\text{m}$ ,  $h_{b1} = 0.081 \mu\text{m}$ , and  $\Lambda = 0.273 \mu\text{m}$ .

The results of calculations for different angles of incidence of light onto the grating are presented in Fig. 2.15.

For the experimental proof of such a possibility the waveguide-grating structure with the same parameters as in Fig. 2.13 but with  $h_f = 0.325 \mu\text{m}$  was prepared. This structure was used as the resonant-reflecting mirror in dye laser. *Rhodamine 6G* dissolved in ethanol was used as a dye. The dye was pumped by the radiation with  $\lambda = 0.53 \mu\text{m}$ . The angular dependence of lasing-action threshold of the dye laser was measured in the experiment. We correlated the obtained angular range of laser tuning with the calculated one. The lasing was obtained in the wavelength range  $\Delta\lambda = 0.55\text{--}0.58 \mu\text{m}$  where the variation of the autocollimation reflectivity of the considered structure is small.

Thus, the analysis of the diffraction of light in the corrugated layer system performed shows that the excitation of the leaky modes in the structure may provide high diffraction efficiency of the grating in the autocollimation regime. In addition, the usage of the leaky modes with  $n^* \approx 1$  allows one to obtain a reasonably broad operating range of spectrum for such waveguide-grating structures. This was confirmed by the numerical

analysis and experiment. Such structure could also be used with tunable  $\text{LiF:F}_2^-$  color center laser in near IR spectral region and provide high reflectivity and good spectral selectivity for narrowline laser operation.

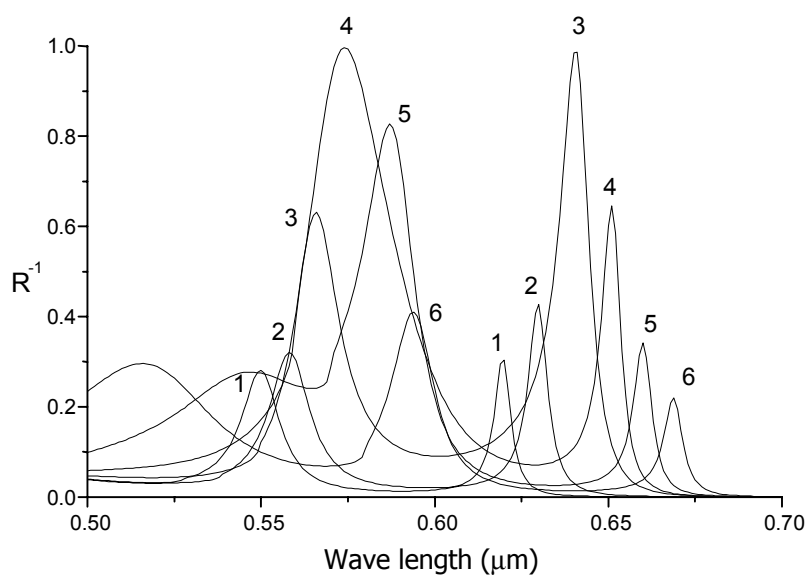


Fig. 2.15. The results of calculations for different incidence angles of light onto the grating. Angle of incidence: 1- 38, 2 – 40, 3 – 42, 4 – 44, 5 – 46, 6 – 48 degrees.

The oscillator setup utilized diffraction gratings as disperse elements in the cavity. Diffraction gratings exhibit unique quality to have high spectral selectivity, large free spectral region between different maxima, simple linear tuning with sine mechanism and the possibility to control absolute wavelength with high accuracy.

The incidence ( $\alpha$ ) and diffraction angles ( $\beta$ ), radiation wavelength ( $\lambda$ ) and grating spacing ( $t$ ) depends are connected by the following diffraction grating equation:

$$t(\sin \alpha + \sin \beta) = m\lambda ,$$

here  $m$  - is a diffraction order. For autocollimation regime when the incidence and diffracted angles are equal to each other ( $\alpha=\beta$ ) this equation becomes

$$2t \sin \alpha = m\lambda .$$

The angular dispersion of the grating in autocollimation scheme equals as:

$$D = 2tg\alpha / \lambda$$

The dispersion of the grating is increased with reducing its spacing  $t$ . Meanwhile the spacing ( $t$ ) is limited and cannot be smaller than  $\lambda/2$ , for smaller spacing the diffraction becomes impossible. For diffraction grating the important values of spacing are

$$\lambda/2 \leq t \leq \lambda \quad \text{or} \quad t \leq \lambda \leq 2t$$

It corresponds to the situation when there is only two reflected beams: the first and zero diffraction orders. For autocollimation scheme this condition becomes as follows:

$$\lambda/2 \leq t \leq 3\lambda/2 \quad \text{or} \quad 2t/3 \leq \lambda \leq 2t$$

The theoretical angular resolution of diffraction grating  $\delta\Theta$  equals

$$\delta\Theta = \lambda / zt \cos \beta$$

Here  $z$  is the number of the grating lines in the illuminated area. For the most part of the tunable lasers  $\delta\Theta$  is much less than the divergence of the incident radiation and doesn't determine the oscillating linewidth. The maximal theoretical resolution of the grating equals to the maximal difference in the optical paths of interference beams and is determined by the following equation:

$$R = \frac{\delta\lambda}{\lambda} = Nt$$

here  $N$  is the total number of the grating grooves. For example for  $1 \mu\text{m}$ , and spacing  $t=0.83 \mu\text{m}$  and diffraction width  $40 \text{ mm}$  the maximal spectral resolution for one pass diffraction equals to  $\delta\nu \approx 0.2 \text{ cm}^{-1}$ . It is necessary to note that in the cavity during the development of the

oscillation the multiple passes can sufficiently reduce the oscillating linewidth till single mode oscillation.

The autocollimation condition is easily obtained from equation  $2t \sin(\alpha) = m\lambda$ . From this equation follows that the oscillation wavelength depends on the incident angle as a *sin* law. Such dependence can be easily realized by *sin* mechanism. This mechanism can realize the linear dependence of the oscillating wavelength and can easily control it. Lets consider in more details the disperse properties of the cavity with the grating. To find the angular dispersion we need use first derivative of this equation with respect to  $\lambda$  at constant  $\alpha$ .

The comparison of autocollimation angle and angular dispersion for three different gratings is shown in Fig. 2.16 for LiF:F<sub>2</sub><sup>-</sup> CCL spectra region. The gold diffraction grating had 800 grooves/mm and its working angle for second order diffraction (1600 grooves/mm) for 1.2  $\mu\text{m}$  operating range is close to grazing incidence scheme (see Fig. 2.16(a)). As can be seen from the Fig 2.16(b) the grating with 1600 grooves/mm has sufficiently higher angle dispersion  $D$  within 1.19-1.2  $\mu\text{m}$  range as compared to diffraction gratings with 1500 and 1200 grooves/mm. The 800 grooves/mm grating (25x25 mm size) is working in the second diffraction order so the output into the first diffraction order should be regarded as losses and thus minimized. For the investigated grating the reflection into the second diffraction order was measured to be about 35% while reflection into the first diffraction order was less than 5% (for horizontal polarization).

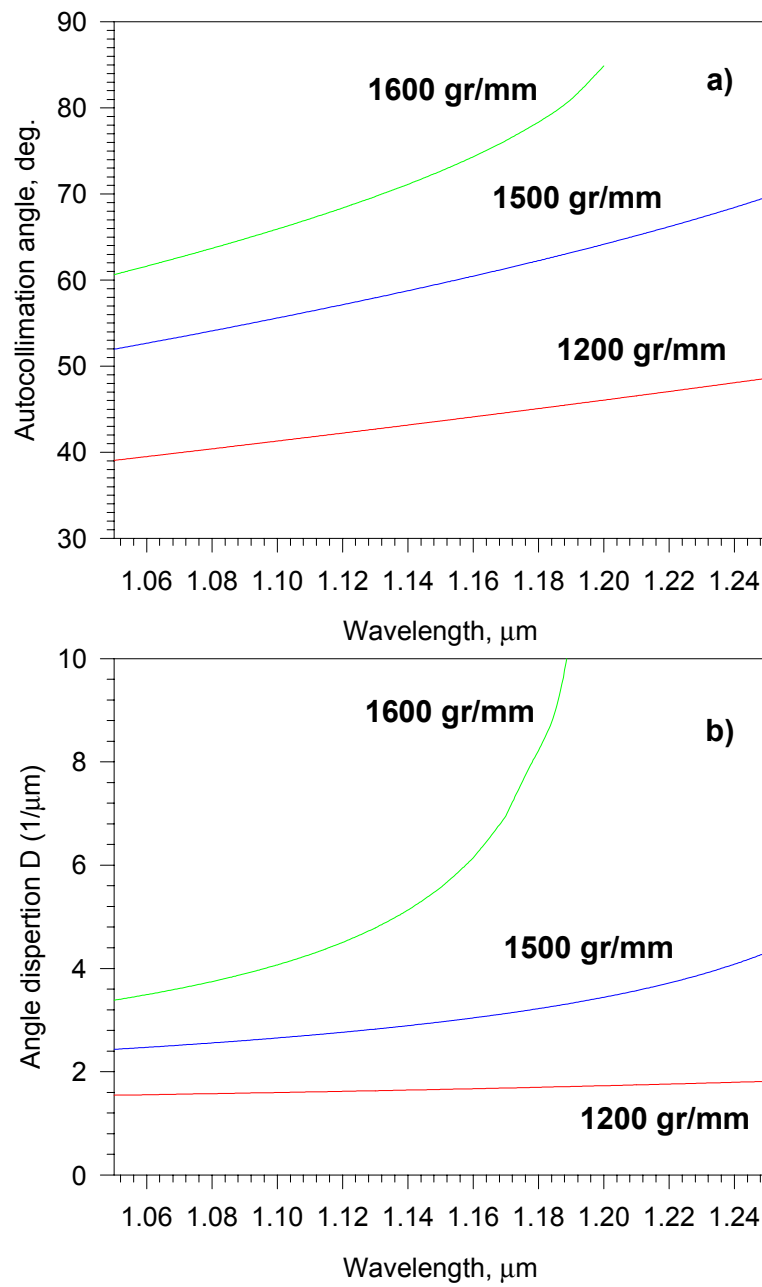


Fig. 2.16. Autocollimation angle versus wavelength (a) and angle dispersion D (b) for gratings with 1600, 1500 and 1200 grooves/mm.

## 2.4. Sine mechanism for diffraction grating scanning

As we have seen in the previous report for narrow line laser oscillation one needs to use the diffraction grating as a spectral selective element. The wavelength scanning of the tunable laser can be arranged by rotating the diffraction grating, that is results in the changing of the incident angle. The condition for autocollimation operation of diffraction grating is as following:

$$\lambda = 2D \sin \Theta$$

Here  $\lambda$  is the oscillating wavelength,  $D$  is the grating spacing, and  $\Theta$  is the incident angle. The angular dependence of the operating wavelength is described by the sinus law. It could be rather complicated to control the oscillating wavelength by direct rotation of diffraction grating. This is the reason why special sinus mechanisms are used in tunable lasers and spectral devices. Such mechanism provides linear dependence of the oscillating wavelength versus the rotation angle of a motor or a handle. Fig. 2.17 presents the scheme of the sine

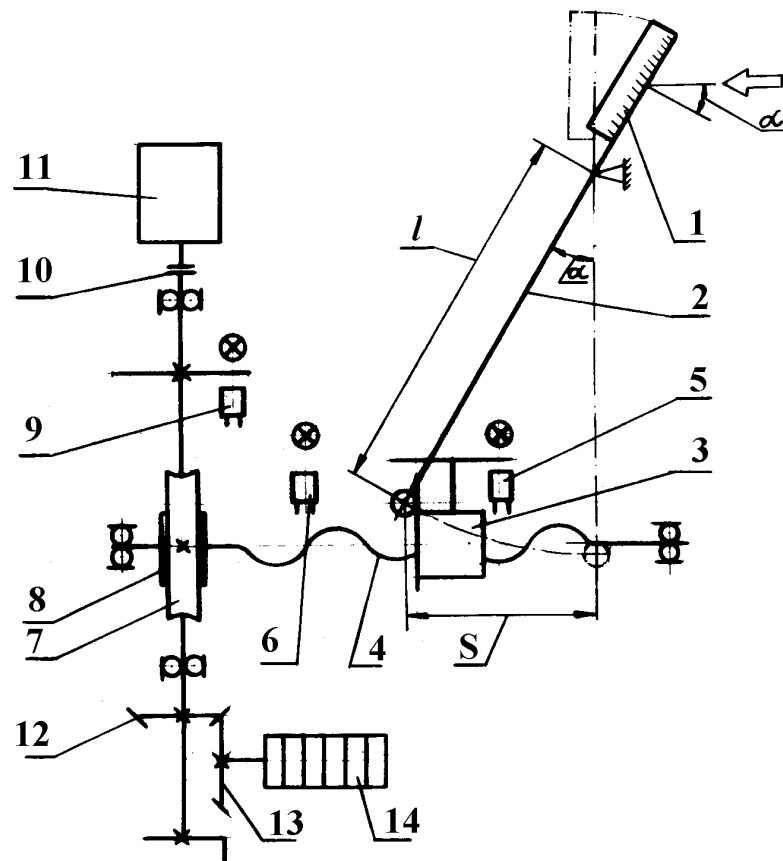


Fig. 2.17. Drawing of the sinus mechanism of diffraction grating drive.

scanning mechanism of tunable laser.

The motion of the step motor 11 is transmitted through the worm gear pair to rotation of the screw 10 over which the nut 7 is travelling. Guide strip 4 is secured to nut 3 by means of screws and aligned with the working surface by means of two pins. The working surface of strip 3 over which the diffraction grating stage lever stop is sliding must be positioned strictly normal to the axis of motion screw 4 by means of adjusting screws. Three ball bearings mounted on the body of nut 4 embrace accurate guide. The gear pair 12,13 provide correct settings on the wavelength counter 14. Due to sine mechanism of diffraction grating drive the value on the counter can be aligned to provide correct wavelength.

The operational wavelength ( $\lambda$ ) can be found by the number of steps ( $n$ ) of the driver from the reference position corresponding to the calibrated wavelength value ( $\lambda_c$ ) by the following equation  $n = (\lambda_c - \lambda) / \Delta\lambda$ . Here  $\Delta\lambda$  is the gear number of the driver. Below the main design relationships of this mechanical diagram are presented.

The sinus mechanism equation is as following:

$$\lambda = 2 \cdot D \cdot S / l,$$

here  $l$  is the length of the lever 2 and  $S$  is the working motion of the nut 3.

The value of one step of the step motor in wavelength:

$$\Delta\lambda = 2 \cdot D \cdot t \cdot \gamma \cdot i / (360 \cdot l),$$

here  $t$  is the pitch of screw 4;  $\gamma$  is the angle at which the step motor turns after one step;  $i$  is the gear ratio of worm gear pair 8 and 7;  $l$  is the length of lever 2.

Following are the numerical values of the parameters specified in the formulas (2) and (3) for the mechanical diagram and the diffraction grating shown in Fig. 2.17 and made in mechanical mounting:

$$D = 1/1200 \text{ 1/mm}, t = 1.5 \text{ mm}, \gamma = 1.8 \text{ deg.}, i = 2/25, l = 100 \text{ mm}$$

Table 1 specifies the sine mechanism parameters for the characteristic wavelengths of the laser unit that can be used for testing and aligning. The values of the parameter  $\delta\alpha$  correspond to the angular turn of the diffraction grating at which the maximum of the oscillating spectrum is tuned at 0.1 nm. In the diffraction grating drive diagram the working motion of the nut ( $S = 38$  mm) provides continuous setting of the wavelengths produced by the diffraction grating in the range from 638 nm to 1265.6 nm. For these spectral range specific points could be positively reproduced by means of a single-mode He-Ne laser. The wavelength ( $\lambda = 632.8$  nm) in the first diffraction order is taken as a wavelength calibration value. Thus, the number of the driver rotations is linearly proportional to the shift of the nut  $S$  and linearly proportional to the operational wavelength.



Table 1. The calculated parameters of the sine mechanism for edge wavelengths of tunable  $\text{LiF:F}_2^-$  color center laser and reference He-Ne laser wavelengths.

$\lambda$ , nm	$\alpha$ , degree	$S$ , mm	$\delta\alpha$ , arc sec
632.8 *	22.3139	37.968	27
1100	41.0999	66.000	33
1240	48.0733	74.400	37
1265.6*	49.4078	75.936	38

\*- 1<sup>st</sup> and 2<sup>nd</sup> diffraction orders of He-Ne laser radiation for 1200 l/mm diffraction grating.

## 2.5. Prism telescope

Narrowline laser operation requires good filling of the selective diffraction grating. One of the solutions is to use prism telescope for intracavity beam expanding. Below we will consider two types of intracavity prism telescopes. The typical configuration of the single prism telescope is shown in Fig. 2.18. To reduce the intracavity losses the prism telescope includes Brewster prisms with anti-reflection (AR) coating. In this case the incident narrow beam enters the longer prism face under Brewster angle and must have zero reflection. The broadened beam transmits perpendicular out of prism face with AR coatings. The telescope factor for the Brewster prism depends on its materials and for normal glass BK-7 is about 1.4 and can be increased by using materials with higher refractive index.

Another possibility to increase the magnification factor is to use two or more prisms in the telescope. Figs. 2.19 and 2.20 present optical schemes of two- and four-prism telescopes which have  $\sim 2$  and  $\sim 4$  telescope magnification factors, correspondingly. The pictures of these telescopes are presented in Figs. 2.21 and 2.22. The first telescope is composed with two Brewster glass prisms with AR coatings and the glass element to compensate the parallel beam displacement in the vertical plane and bring it back to the same optical axis. The second telescope includes four Brewster glass prisms with AR coatings. It provides the constant direction of the transmitted radiation.

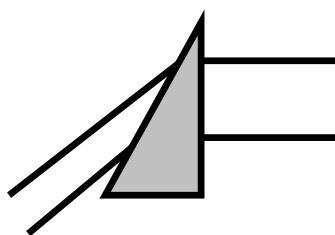


Fig. 2.18. Single prism telescope.

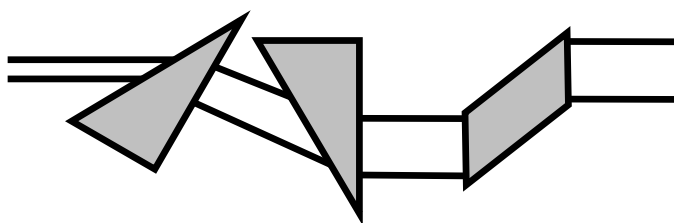


Fig. 2.19. Optical scheme of two-prism telescope with compensation of displacement.

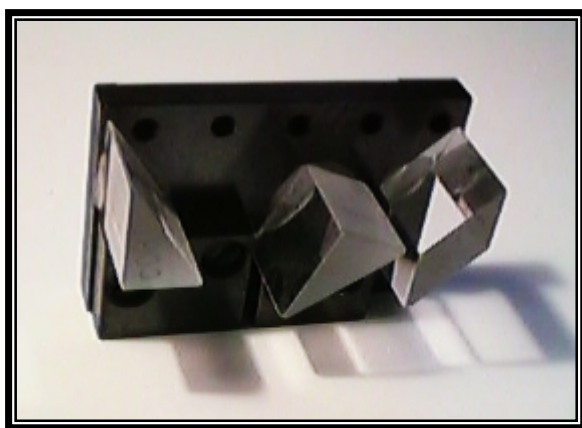


Fig. 2.20. Design of two-prism telescope.

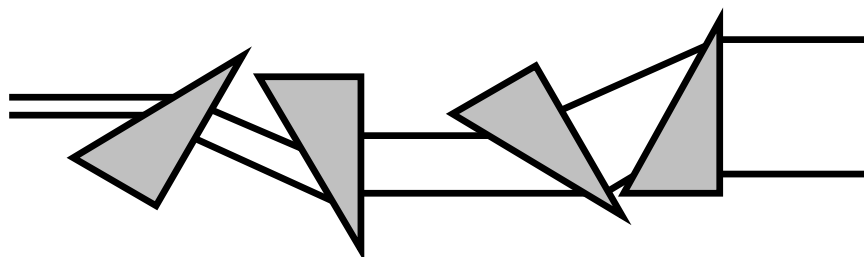


Fig. 2.21. Optical scheme of four-prism telescope.



Fig. 2.22. Design of four-prism telescope.

Another optical scheme of solid two-prism beam expander for CCL mockup is presented in Fig. 2.23. To prevent the origin of laser oscillation at the faces of the prisms the angular parameters prism positions were slightly modified. The radiation incidence angle at the back faces of the prisms in expander was made to be equal  $3^\circ$  to the normal. To make the expander compact and easy in use it was designed as integrated nonadjustable unit. The realization of such expander is presented in Fig. 2.24.

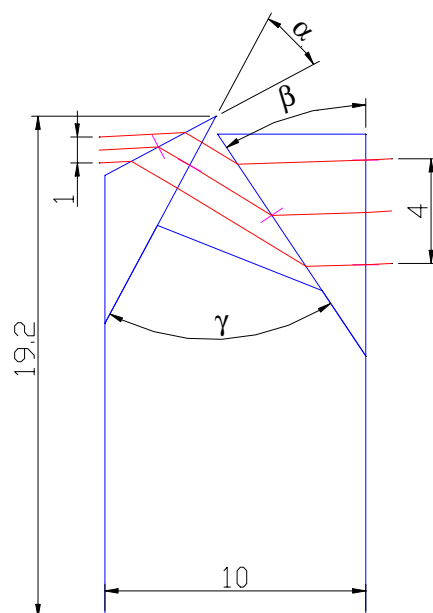


Fig. 2.23. Optical scheme of two-prism telescope.



Fig. 2.24. Solid two-prism telescope.

### 2.6. Prism and mirror holder

In the laser unit number of prisms and HR mirrors are used to deliver pump laser beam to the color center crystal. For its precise alignment we need to have special mountings. The drawing and picture of the specially developed prism or mirror holder are shown in Figs. 2.23, 2.24. The mounting has variable possibilities of aligning. If the laser beam axis is

displaced from the center of the prism then it is possible to ease off screws 10 and move the mounting base. To rotate the prism one needs to ease screws 2 and to turn the base with the prism around the mountain axis. If the laser beam transmits upward or downward, it is necessary to unscrew 8 and tighten 9 vice versa until the beam will have appropriate altitude alignment. The last procedure can require the consequent angular alignment.

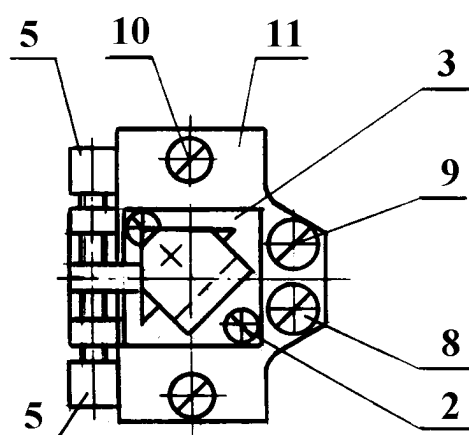


Fig. 2.23. The drawing of the prism holder.

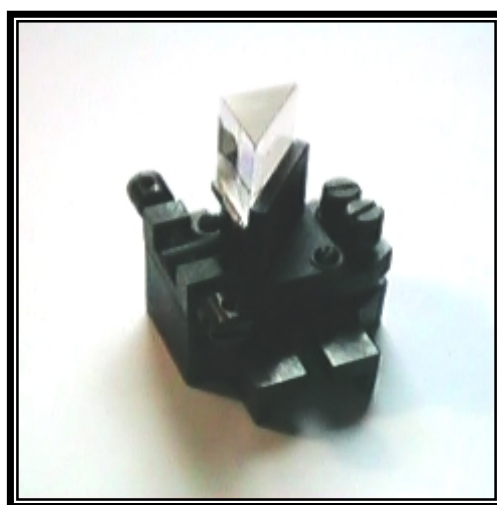


Fig. 2.24. The picture of the prism holder.

## 2.7. Fabri Perrot etalon

One of the ways to narrow the spectral line of tunable laser is to use intracavity Fabri-Perrot etalon. Three solid state etalons were tested in our experiments. The etalon is characterized by its thickness and the reflectivity of its faces. The thickness ( $t$ ) determines the Free Spectral Range (FSR) of the etalon and is described by the following equation:  $FSR = (2 \cdot n \cdot t)$ , here  $n$  is the refractive index of the substrate. The finesse of the etalon determines its spectral resolution. The higher the reflectivity – the larger the finesse. At the same time it is necessary to keep in mind that the higher the reflectivity of the etalon – the larger the intracavity losses and lower the efficiency of the laser. Below we present parameters of glass Fabri-Perrot solid etalons specially prepared for  $\text{LiF:F}_2^-$  color center laser mock-up. Fig. 2.25 presents the design of the etalon with the mounting.

Table 2. Parameters of Fabri-Perrot etalons tested in the tunable  $\text{LiF:F}_2^-$  color center laser.

No.	Thickness [mm]	Reflectivity [%]	FSR [cm <sup>-1</sup> ]	Finesse
1	1	60	5	6
2	1	85	5	20
3	2	85	2.5	20



Fig. 2.25. Fabri-Perrot etalon in the mounting.

## 2.8. Output coupling mirror

Output coupling mirror ( $M_3$ ) is very important to provide high oscillator efficiency and required tunable spectral range. Our earlier investigation [6] showed that in order to increase laser efficiency at the edges of the tuning curve and extend its spectral range higher reflectivity output couplers should be used. Fig. 2.26 presents theoretical tuning curves of  $\text{LiF:F}_2^-$  CCL with 10%, 20%, 50%, 70% and 90% reflectivity output couplers when pumped with  $\text{Nd}^{3+}$ :YAG laser. The highest laser efficiency is observed for 20-50% reflectivity output coupler. The increase of output coupler reflectivity results in broadening of the tuning spectral range of  $\text{LiF:F}_2^-$  CCL to longer wavelengths up to 1310 nm. The short wavelength edge was limited by 1064 nm pump laser wavelength.

Thus, to obtain high conversion efficiency and broad tuning range one needs to use output coupler with smooth spectral profile and about 20-40% reflectivity. The spectrum of the used mirror  $M_3$  is shown in Fig. 2.27. To work at the edges of the tuning curve one needs to increase output coupler reflectivity at the desired wavelength. Our earlier investigation [6] doesn't consider two-pass superfluorescence in CCL which occurs with the reflection from the output coupler and limits oscillations at the edges of the tuning curves. To reduce this effect we need to use output couplers with low reflectivity in the maximum of the tuning curve.

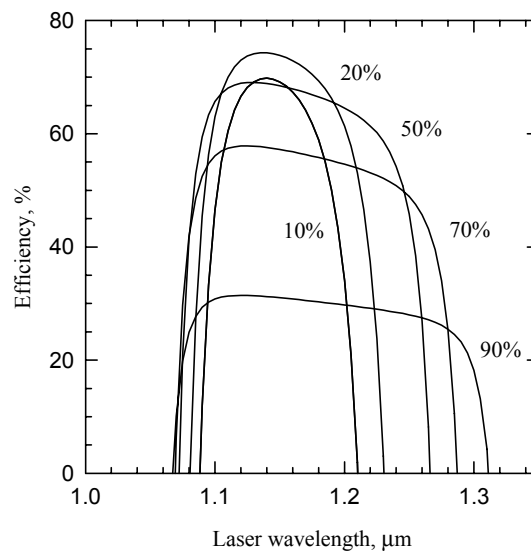


Fig. 2.26. Theoretical tuning curves of  $\text{LiF:F}_2^-$  CCL with various reflectivity output couplers  $R=10\%$ ,  $20\%$ ,  $50\%$ ,  $70\%$ ,  $90\%$ .

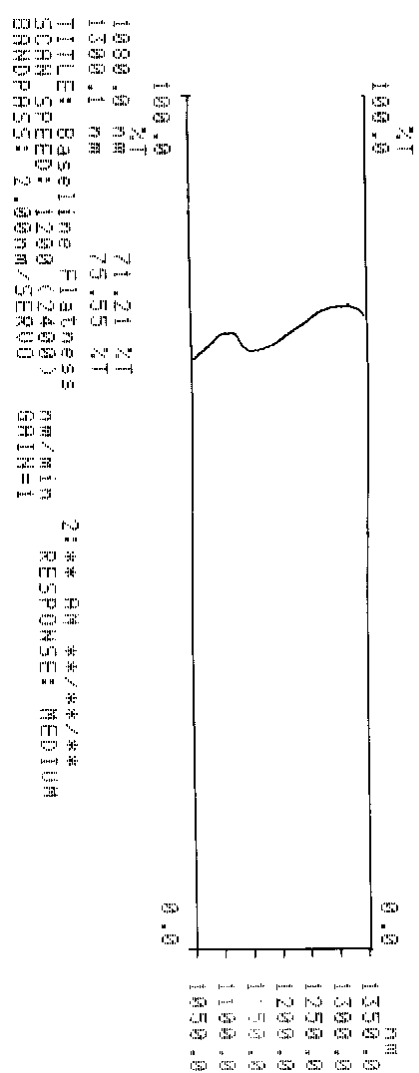


Fig. 2.27. Transmission spectra of the cavity output coupler used in the setup.



The realization of  $\text{LiF:F}_2^-$  color center laser mockup is presented in Fig. 2.28. Optical elements are mounted on the steel stage. A He-Ne laser is located in the lower compartment of the unit and allows aligning of all optical elements and wavelength calibration. Its switch is located in the right part of the front panel. The handles provide manual scanning of diffraction grating and Fabri Perrot etalon. Their automatic control is arranged with step motor driver and PC controlled board. Wavelength counter shows the operating wavelength of the laser with the accuracy  $\pm 1 \text{ \AA}$ .

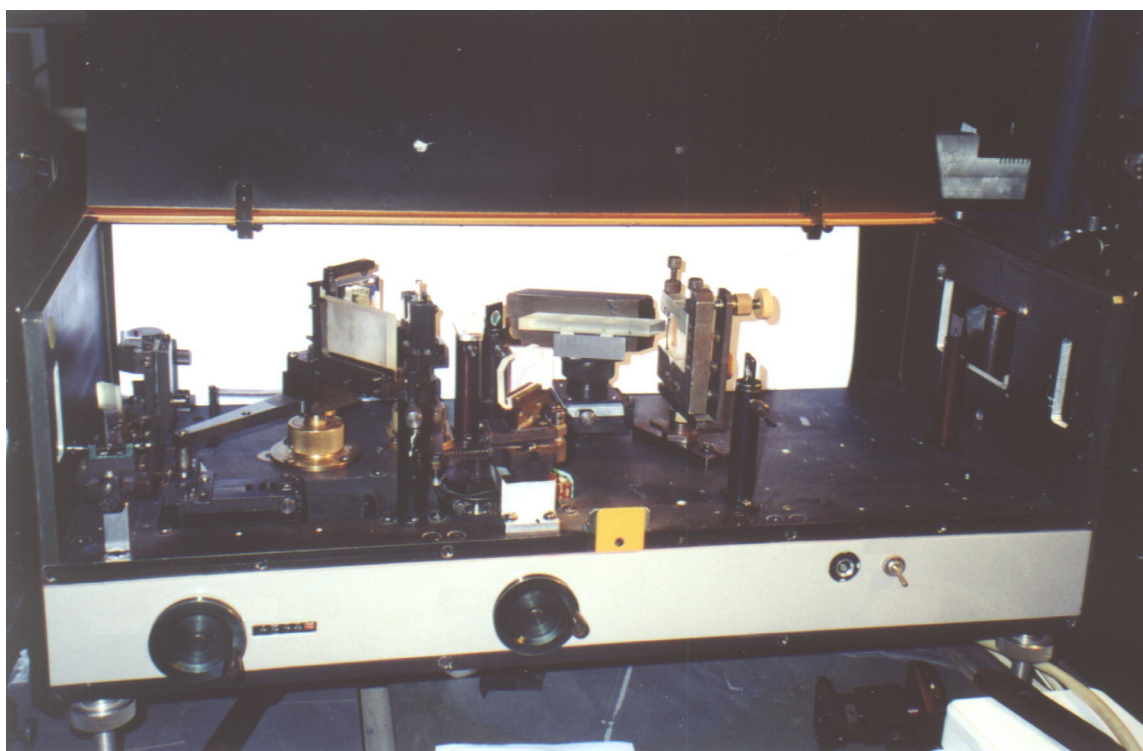


Fig. 2.28.  $\text{LiF:F}_2^-$  color center tunable laser oscillator.

The operation of  $\text{LiF:F}_2^-$  color center oscillator was tested with  $\text{Nd}^{3+}:\text{YLiF}_4$  pumping. The experimental setup for investigation of spectral and energy parameters of  $\text{LiF:F}_2^-$  color center oscillator mockup is shown in Fig. 2.29. The output laser energy was measured by energymeter IMO-2H. To measure the exact wavelength the laser output radiation was measured by precise wavelength meter developed in General Physics Institute. The wavelength meter is based on four Fizo interferometers with increasing thickness each combined with CCD readout system. The accuracy of wavelength measurement depended on the laser linewidth and the number of interferometers in use. For laser linewidth

$0.5 \div 0.05 \text{ cm}^{-1}$  three interferometers were in use that corresponded to the accuracy of  $0.1 \div 0.02 \text{ \AA}$  in the working region. For narrower linewidth, when all four interferometers operated the accuracy of wavelength meter was increased to  $0.005 \div 0.002 \text{ \AA}$ . The readout system based on silicon CCD matrix was tested to be sensitive for laser radiation up to 1190 nm wavelength. To register spectral properties of longer wavelengths we used crystalline  $\text{LiNbO}_3$  second harmonic doubler.

Spectral linewidth of  $\text{LiF:F}_2^-$  CC oscillator mockup was measured at different parts of the tuning curve. An example of spectral profile measured with fourth Fizo interferometer at 1250 nm wavelength is shown in Fig. 2.30. The linewidth was measured to be less than 500 MHz.

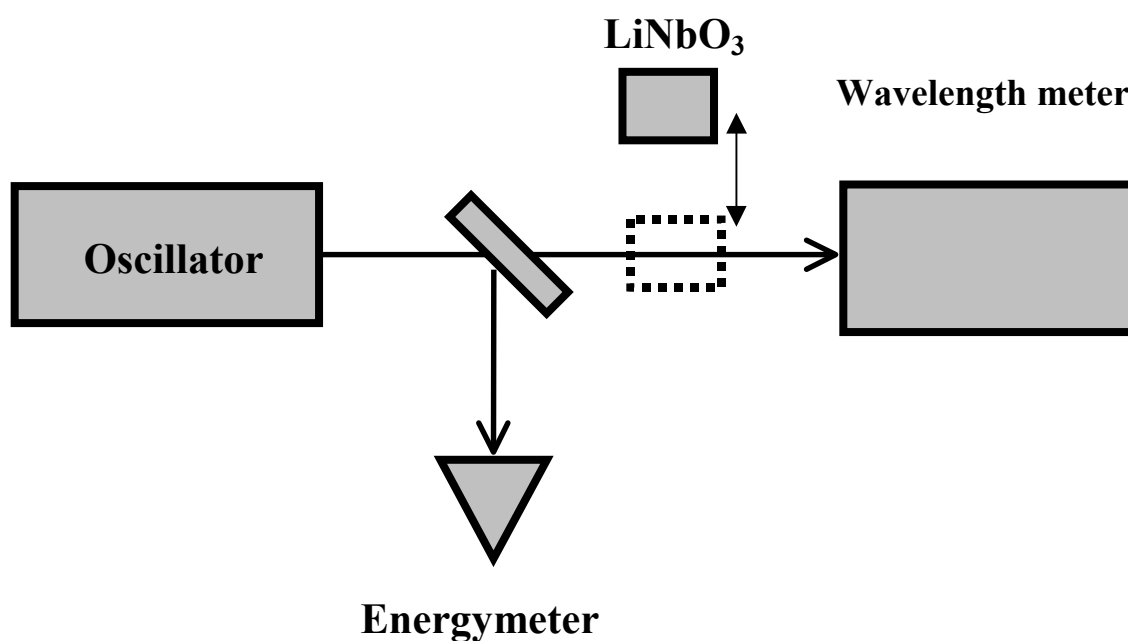


Fig. 2.29. The experimental setup for investigation spectral and energy parameters of  $\text{LiF:F}_2^-$  color center oscillator.

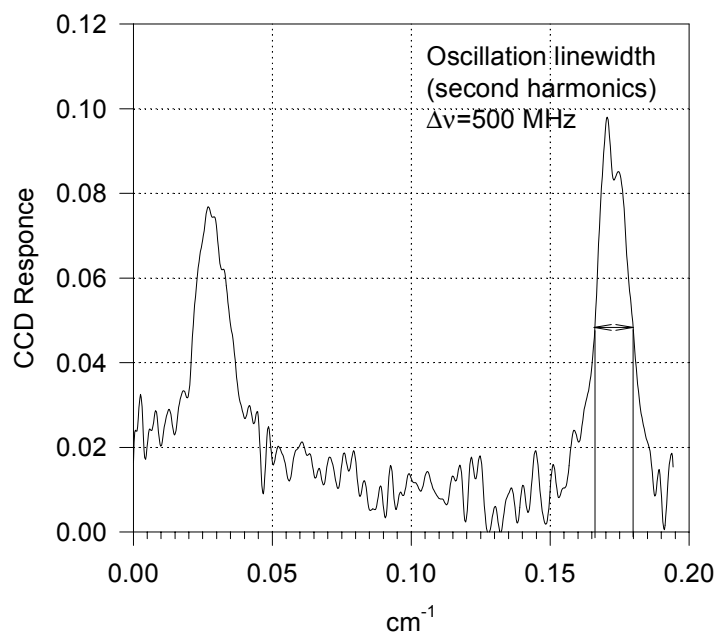


Fig. 2.30. Spectral profile of LiF:F<sub>2</sub><sup>-</sup> color center oscillator laser narrow line measured by fourth Fizeau interferometer of wavelength meter.

### 3. Color center energy and power amplifier

In order to amplify weak radiation with special spectral, spatial and temporal properties to high peak power one needs to use powerful amplifier. High emission cross section of  $F_2^-$  color centers ( $\sigma_{em} = 7 \cdot 10^{-17} \text{ cm}^2$ ) and lifetime equaled to 55 ns allows to propose high amplification gain and efficiency of  $\text{LiF:F}_2^-$  amplifier. Comparing with dye solutions the concentration of  $F_2^-$  color centers in LiF crystal is rather low. Due to this the longitudinally pumped amplifier scheme is preferable for good spatial overlapping of the pump and probe radiation in the bulk color center crystals 40 and 80 mm long.

Below the results on testing the amplification characteristics of  $\text{LiF:F}_2^-$  color center crystal under pulsed  $\text{Nd}^{3+}:\text{YAG}$  and  $\text{Nd}^{3+}:\text{YLiF}_4$  pumping to use it in MOPA schemes. The amplification in  $\text{LiF:F}_2^-$  color center crystal was tested in single-pass and double-pass optical schemes.

#### 3.1. $\text{LiF:F}_2^-$ amplifier with $\text{Nd}^{3+}:\text{YAG}$ pumping

##### Single-pass scheme

Experimental setup for single-pass amplification included pulsed  $\text{Nd}^{3+}:\text{YAG}$  laser with output energy up to 100 mJ, 10 ns pulse duration, 3 pps pulse repetition rate (Fig. 3.1). Tunable  $\text{LiF:F}_2^-$  color center laser (CCL) provided tunable nanosecond probe beam with smooth spatial profile and low angular divergence. Due to high luminescence cross section of  $F_2^-$  color centers and high reflectivity output coupler (several tunable laser cavity round trip times) the probe radiation pulse was delayed for only  $2 \div 6$  ns from the pump pulse that required short optical delay line of  $0.5 \div 2$  m for the amplifier pump pulse. Neutral density glass filters varied the energies of probe and pump beams. The energies of pump, probe and amplified pulses were registered by photodiodes connected to Tektronix digital oscilloscope that allowed simultaneous measurement of all the pulses. High power beams were measured with IMO-2H joulemeter.

The important factor for efficient amplification is good temporal overlapping of the pump and probe pulses. In our experiments the change of the optical delay between the two beams varied the temporal delay of the probe pulse. Three temporal cases were considered: synchronous pulses ( $\Delta t = 0$ ), small delay of the probe pulse ( $\Delta t = 1.5$  ns) and large delay of the probe pulse ( $\Delta t = 5$  ns), Fig. 3.2. Due to high amplification in  $\text{LiF:F}_2^-$  CCL active medium the probe pulse duration was slightly shorter than that of the pump and was about

8 ns. The results of the single-pass amplification in  $\text{LiF:F}_2^-$  crystal 90 mm long with Brewster cut faces for three temporal cases with pump energy 40 mJ are summarized in Fig. 3.2. One can see that the highest amplification was observed for small temporal delay  $\Delta t = 1.5$  ns.

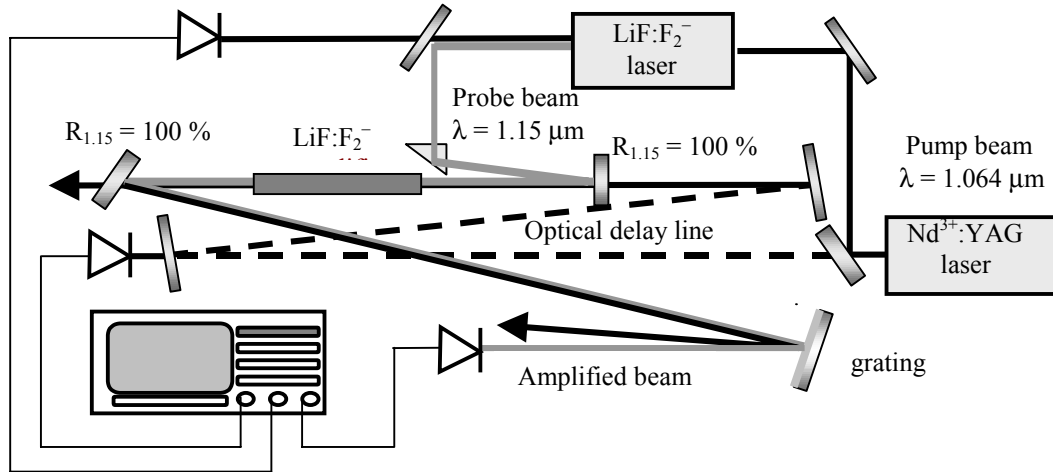


Fig. 3.1. Experimental setup for investigation the single-pass  $\text{LiF:F}_2^-$  color center amplifier.

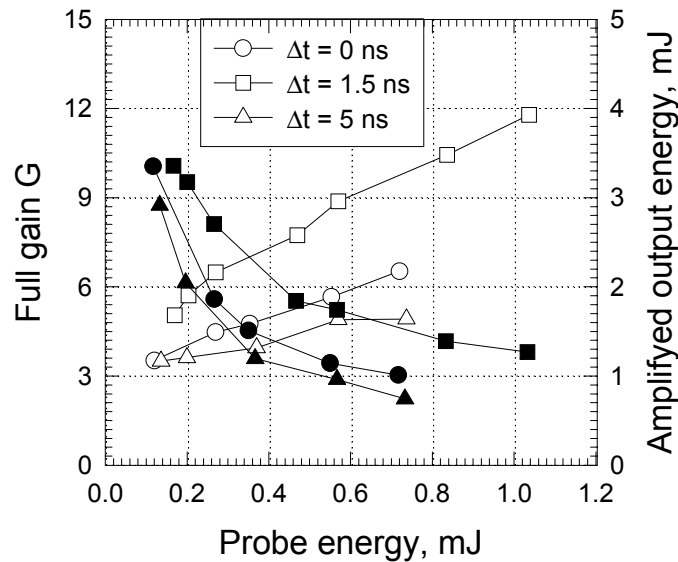


Fig. 3.2. Output energy and amplification gain versus probe energy for three temporal delays (0, 1.5, 5 ns) in single-pass amplification experiments.

The initial part of the pump pulse is used for excitation of  $F_2^-$  color centers and the saturation of absorption in the active channel. The required time depends on the pump power density and the temporal shape of the front edge of the pulse. After the absorption saturation the medium provide efficient amplification of the probe pulse. If the probe pulse arrives synchronously ( $\Delta t = 0$ ), its amplification is reduced due to low excitation at the beginning of the pulse. If the probe pulse comes later ( $\Delta t = 5$  ns), the amplification is lower due to the decrease of the pump power level. The proper delay between the pump and the probe pulses can result in high energy conversion efficiency that could be even higher than that in  $LiF:F_2^-$  CCL due to low contribution of the cavity and active medium passive losses.

The output energy and gain dependencies of the single-pass amplification in  $LiF:F_2^-$  color center crystal 40 mm long with initial absorption coefficient  $K(1.064) = 0.67 \text{ cm}^{-1}$  and 40 mJ pump pulse energy are shown in Fig. 3.3. The highest amplification gain value of  $G = 12$  was obtained for low probe pulse energy ( $E_{\text{probe}} = 0.06 \text{ mJ}$ ). The increase of the probe pulse energy up to 1 mJ resulted in the saturation of the amplification with lowering the amplification gain to  $G = 4$  and increasing the output energy up to 4 mJ per pulse. This value corresponded to about 10% energy conversion efficiency of  $LiF:F_2^-$  color center amplifier.

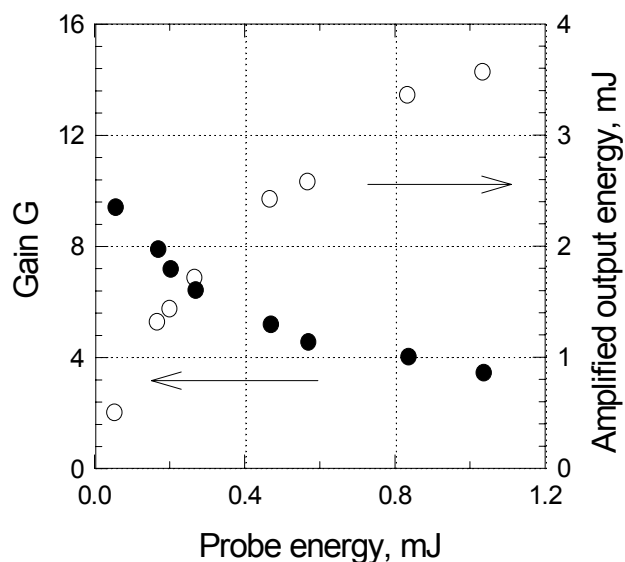


Fig. 3.3. Energy dependencies of the amplification gain and the output energy of  $LiF:F_2^-$  single-pass color center amplifier with 40 mJ pump pulse.

### Double-pass scheme

Double-pass scheme enlarges the interaction length of the amplifier medium that results in the increase of the amplification gain. The optical scheme of experimental setup for double-pass amplification experiments is shown in Fig. 3.4. The scheme was based on the same  $\text{Nd}^{3+}:\text{YAG}$  laser. Due to additional HR mirror the pump and probe beams passed twice through the investigated sample. Small intersection angle inside the sample equaled  $2^\circ$  and allowed to obtain good spatial overlapping.  $\text{LiF:F}_2^-$  sample 88 mm long with Brewster cut faces and initial absorption  $K(1.064) = 0.45 \text{ cm}^{-1}$  was used in these experiments.

The dependence of the amplification on the focusing conditions of the pump beam was investigated with pump pulse energy 72 mJ. Fig. 3.5 presents the amplification gain for three diameters of the pump beam: without focusing,  $\varnothing = 3 \text{ mm}$  (circles); with telescope collimation,  $\varnothing = 2 \text{ mm}$  (squares); and telescope broadening,  $\varnothing = 4 \text{ mm}$  (triangles). The collimation of the pump beam could speed-up the saturation process and increase pump to probe conversion efficiency. At the same time this can reduce the intersection volume of the pump and probe beams. Fig. 3.5 shows that for our experimental conditions the maximal amplification gain ( $G \sim 4$ ) and energy conversion efficiency up to 20% was obtained without pump beam focusing.

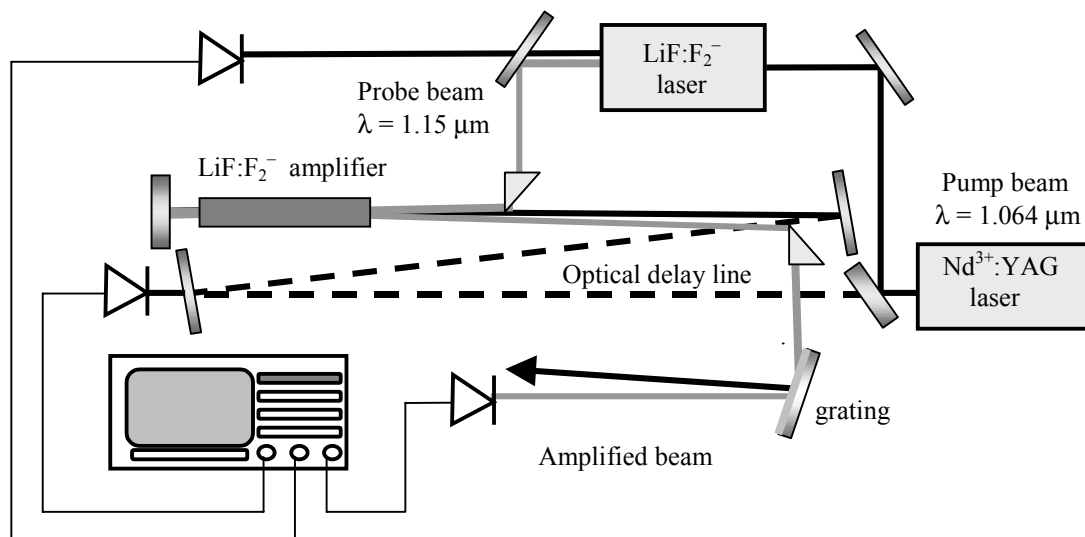


Fig. 3.4. Experimental setup for investigation the double-pass  $\text{LiF:F}_2^-$  amplifier scheme.

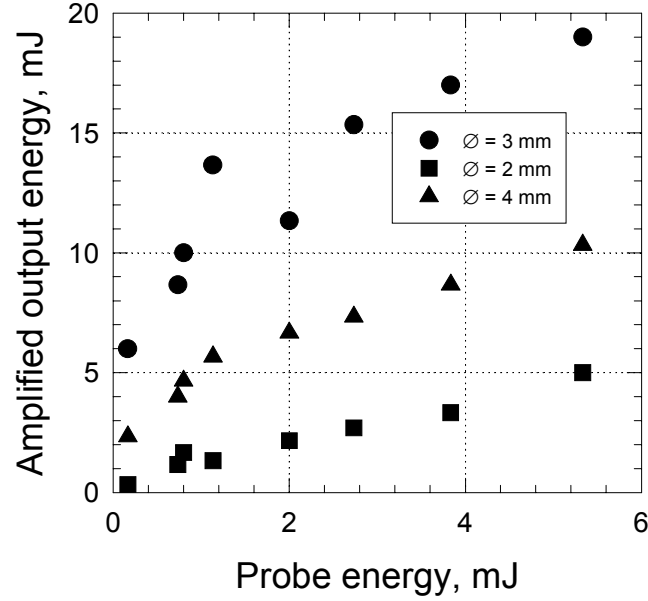


Fig. 3.5. Amplification in double-pass  $\text{LiF:F}_2^-$  color center amplifier for three pump beam collimating condition: without collimating ( $\varnothing = 3$  mm), with collimating ( $\varnothing = 2$  mm) and with beam broadening ( $\varnothing = 4$  mm) at  $E_{\text{pump}}=72\text{mJ}$ .

Fig. 3.6 shows the best results on the amplification in  $\text{LiF:F}_2^-$  color center crystal 88 mm long for 40 mJ pump pulse energy in double-pass scheme. For low energy incident probe pulse (0.08 mJ) the highest amplification gain of 56 was realized which provided 4.2 mJ output energy in the amplified pulse with conversion efficiency about 10%. For higher energy probes (2.2 mJ) the color center amplifier output energy increased to 12 mJ with pump conversion efficiency up to 25% that was close to the best values of CCL conversion efficiency with  $\text{Nd}^{3+}:\text{YAG}$  pumping.

### 3.2. $\text{LiF:F}_2^-$ double-pass amplifier with $\text{Nd}^{3+}:\text{YLiF}_4$ pump laser

Previously it was shown that the use of shorter wavelength pump source based on concentrated neodymium phosphate glass  $\text{Nd}^{3+}:\text{CNPG}$  (1.053  $\mu\text{m}$ ),  $\text{Nd}^{3+}:\text{YLiF}_4$  crystal (1.047  $\mu\text{m}$ ), or  $\text{Nd}^{3+}:\text{LaF}_3$  crystal (1.04  $\mu\text{m}$ ) can significantly increase the conversion efficiency of CCL. In our experiments  $\text{Nd}^{3+}:\text{YLiF}_4$  laser with up to 100 mJ output pulse energy, 13 ns pulse duration and 3 pps repetition rate was used as a pump source. The experimental setup was the same as that used in double-pass amplification scheme (Fig. 3.4).



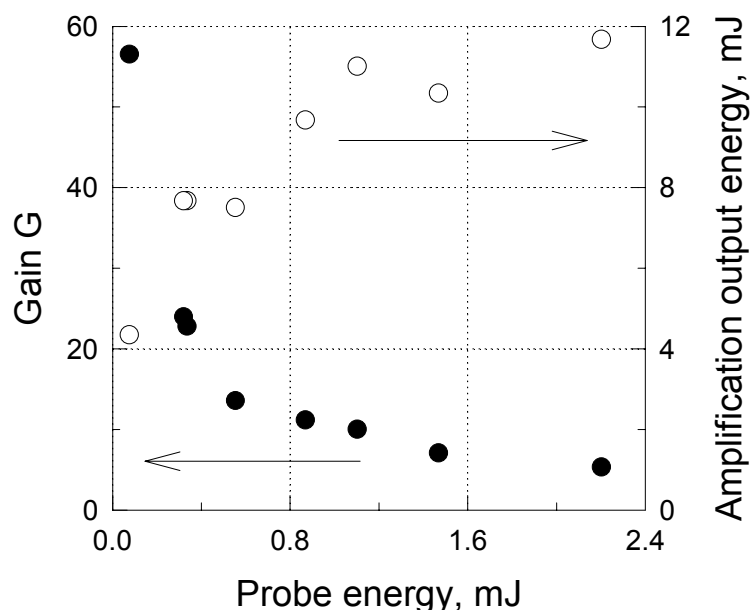


Fig. 3.6. Energy dependencies of amplification gain and output energy of  $\text{LiF:F}_2^-$  double-pass amplifier with 40 mJ pump pulse from  $\text{Nd}^{3+}$ :YAG laser.

The pump and the probe beams passed twice through the investigated sample 88 mm long with initial absorption coefficient  $K(1.047) = 0.72 \text{ cm}^{-1}$ .

The amplification of  $\text{LiF:F}_2^-$  double-pass amplifier with 80 mJ  $\text{Nd}^{3+}$ :YLiF<sub>4</sub> pump was much higher than that for  $\text{Nd}^{3+}$ :YAG pump. Dependencies of the amplification gain and the output energy with respect to the probe energy are shown in Fig. 3.7. The highest amplification gain value  $G = 300$  was obtained for low energy probe pulse of 0.1 mJ. Maximal amplified output energy of 34 mJ with amplification gain  $G = 90$  and energy conversion efficiency 45% was obtained for high energy probe pulse of 0.6 mJ.

Thus, our experimental testing showed that the double-pass  $\text{LiF:F}_2^-$  amplifier with double-pass pumping scheme provide as high as 25% conversion efficiency for 40 mJ pump energy and  $\lambda = 1.064 \text{ }\mu\text{m}$  wavelength. That is 3 times higher than that in collinear single-pass scheme.

Investigation of amplification gain on temporal and spatial overlapping of the pump and probe pulses showed that for our experimental arrangements the highest amplification was observed for 1.5 ns temporal delay of the probe pulse and similar diameters of the beams.

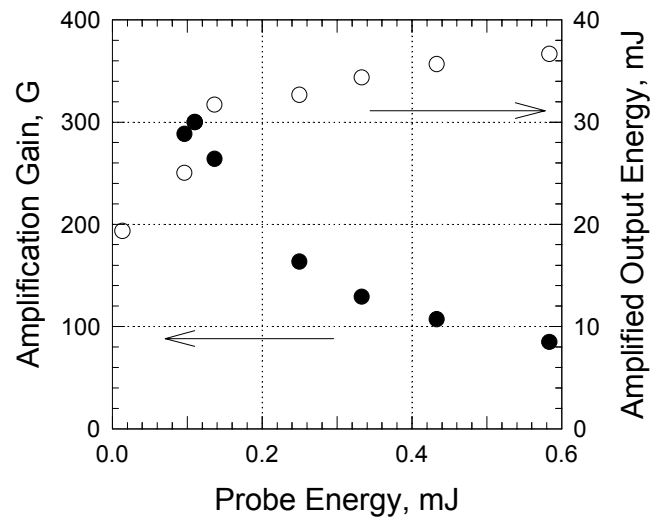


Fig. 3.7. Energy dependencies of the amplification gain and the output energy of  $\text{LiF:F}_2^-$  double-pass amplifier with 80 mJ  $\text{Nd}^{3+}:\text{YLiF}_4$  pump pulse.

The best amplification results were obtained using pulsed  $\text{Nd}^{3+}:\text{YLiF}_4$  laser ( $\lambda = 1.047 \mu\text{m}$ ,  $E=80 \text{ mJ}$ ) as a pump radiation source in double-pass amplification scheme (Fig.3.7). In this case maximum amplified output energy of 34 mJ with amplification gain  $G = 90$  and energy conversion efficiency 45% were obtained for probe pulse energy of 0.6 mJ.

Fig. 3.8 presents the real arrangement of amplifier set consisting of  $\text{LiF:F}_2^-$  color center crystal and HR mirror. The active element was 88 mm long with Brewster cut faces is installed on the crystal mounting. Its initial absorption coefficient at  $1.047 \mu\text{m}$  wavelength was  $0.72 \text{ cm}^{-1}$ . The mirror has reflectivity more than 98% at  $1.047$  and  $1.1\div 1.25 \mu\text{m}$  wavelengths. The pump and amplified beams are reflected from this mirror and have two passes through LiF crystal. This allows to obtain high output after amplifier.

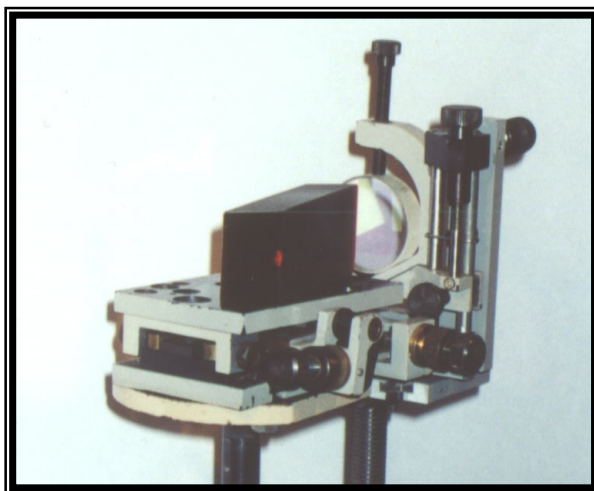


Fig. 3.8. Picture of real arrangement of LiF:F<sub>2</sub><sup>-</sup> double-pass amplifier.

### References:

1. T. T. Basiev, S. B. Mirov, V. V. Osiko, Room-temperature color center lasers, *IEEE J. of Quantum Electronics*, **24**, 1052-1069 (1988).
2. Room temperature tunable color center lasers T. T. Basiev, S. B. Mirov, *Laser Science & Technology book Ser.*, **16**, 1-160, V. S. Letokhov, C. V. Shank, Y. R. Shen, H. Walter, Eds., Gordon and Breach Science Publ./Harwood Acad. Publ. (1994).
3. T. T. Basiev, B. V. Ershov, S. B. Kravtsov, S. B. Mirov, Color center LiF laser with output energy of 100 J, *Sov. J. Quantum Electron.*, **15**, 745-746 (1985).
4. T. T. Basiev, S. V. Dolzhenko, B. V. Ershov, S. B. Kravtsov, S. B. Mirov, V. A. Spiridonov, V. V. Fedorov, LiF:F<sub>2</sub><sup>-</sup> laser parameter optimization for Nd laser pumping, *Bull. Acad. Sci. USSR, Phys. Ser.* **52**, 164-166 (1988).
5. M. G. Littman and H. J. Metcalf, *Applied Optics* **17**, 2224 (1978).
6. T. T. Basiev, P. G. Zverev, A. G. Papashvili, V. V. Fedorov, Temporal and spectral characteristics of a tunable LiF:F<sub>2</sub><sup>-</sup> color center crystal laser, *Quantum Electronics* **27**, 574-578 (1997).
7. Yu. L. Gusev, S. I. Marennikov, V. P. Chebotaev, *Bull. Acad. Sci. USSR, Phys. Ser.*, **44**, 15 (1980).
8. I.A.Parfianovich, V.M.Khulugurov, B.D.Lobanov, and N.T.Maksimova, Luminescence and stimulated emission of color centers in LiF, *Bull. Acad. Sci. USSR, Phys. Ser.*, **43**, 20-27 (1979).
9. W. Gellermann *J. Phys. Chem. Solids*, **52**, 249 (1991).
10. L. F. Mollenauer, Color Center Lasers, in *Tunable Lasers*, L.F.Mollenauer and J.C. White (Eds.), Vol. 59, pp. 225-277, Berlin, New York: Springer Verlag (1987).
11. V. A. Archandelskaya and P. P. Feofilov, *Sov. J. Quantum Electron.*, **7**, 657 (1980).
12. E.F.Martynovich, V.I.Baryshnikov, V.A.Grigorov, Visible lasing of Al<sub>2</sub>O<sub>3</sub> color center crystals at room temperature, *Opt. Commun.*, **53**, 257-258 (1985).
13. A.P.Voytovich, V.A.Grinkevich, V.S.Kalinov, S.A.Mikhnov, Spectroscopic and oscillation characteristics of color center sapphire crystals in the range of 1.0 μm, *Kvant.Electron.*, **15**, 318-320 (1988); *Sov. J. Quantum Electron.* (1988).
14. S.C.Rand, L.G.DeShazer, Visible color-center laser in diamond, *Opt.Lett.*, **10**, 481-483 (1985).
15. A.P.Shkadarevich, A.P.Yarmolkevich, New laser media on color center compound fluoride, *Inst.Phys.AN BSSR, Minsk, USSR*, preprint 24 (1985).

16. A.P.Shkadarevich, A.P.Yarmolkevich, New laser media on color center compound fluoride, *Inst.Phys.AN BSSR, Minsk, USSR*, preprint 24 (1985).
17. T. T. Basiev, F. A. Vakhidov, S. B. Mirov, Radiational transformations in a new  $\text{LiYF}_4$  laser crystal with color centers, *Sov Phys. Lebedev Inst. Reprint*, **7**, 1-5 (1988).
18. L.F.Mollenauer, Color center lasers in *Quantum Electronics*, Part.B, vol. 15, Ch.6, C.L.Tang, Ed., New-York: Academic press (1979).
19. R.E.Rzepka, M.Bernard, S.Lefrant, H.Dubost, R.Charneau, Y.P.Galaup, Laser performance of  $\text{F}_A(\text{II})\text{Li}$  centers prepared by electrolytic coloration in Li-doped KCl crystals, *Opt. Commun.* **62**, 174-178 (1987).
20. Ch.B. Lushchik, I.K. Vitol and M.A. Elango, Decay on electronic excitation of radiational defects in ionic crystals, *Uspehi Fizicheskikh Nauk*, **122**, 223-252 (1977); *Sov. Achievements Physi. Sci.*, (1977).
21. C.J. Delbecq, A study of M center formation in additively coloured KCL, *Z. Phys.*, **171**, 560-581 (1963).